Wind-driving protostellar accretion discs – II. Numerical method and illustrative solutions

Raquel Salmeron,[1,2]* Arieh Königl[2] and Mark Wardle[3]

[1]*Research School of Astronomy & Astrophysics and Research School of Earth Sciences, The Australian National University, Canberra, ACT 0200, Australia*
[2]*Department of Astronomy & Astrophysics and The Enrico Fermi Institute, The University of Chicago, Chicago, IL 60637, USA*
[3]*Department of Physics and Astronomy, Macquarie University, Sydney, NSW 2109, Australia*

ABSTRACT

We continue our study of weakly ionized protostellar accretion discs that are threaded by a large-scale magnetic field and power a centrifugally driven wind. It has been argued that there is already evidence in several protostellar systems that such a wind transports a significant fraction of the angular momentum from at least some part of the disc. We model this situation by considering a radially localized disc model in which the matter is everywhere well coupled to the field and the wind is the main repository of excess angular momentum. We consider stationary configurations in which magnetic diffusivity counters the shearing and advection of the magnetic field lines. In Wardle & Königl we analysed the disc structure in the hydrostatic approximation (vertical motions neglected inside the disc) and presented exact disc/wind solutions for the ambipolar diffusivity regime. In Königl, Salmeron & Wardle (Paper I) we generalized the hydrostatic analysis to the Hall and Ohm diffusivity domains and used it to identify the disc parameter sub-regimes in which viable solutions with distinct physical properties can be expected to occur. In this paper we test the results of Paper I by deriving full numerical solutions (integrated through the sonic critical surface) of the disc equations in the Hall domain. We confirm all the predictions of the hydrostatic analysis and demonstrate its usefulness for clarifying the behaviour of the derived solutions. We further show that the outflow solutions can be extended to larger scales (so that, in particular, they also cross the Alfvén critical surface) by matching the localized disc solutions to global 'cold' wind solutions of the type introduced by Blandford & Payne. To facilitate this matching, we construct a library of wind solutions for a wide range of wind model parameters; this library is made available to the community. The results presented in Wardle & Königl, Paper I and this work combine to form a comprehensive framework for the study of wind-driving accretion discs in protostellar and other astrophysical environments. This theoretical tool could be useful for interpreting observations and for guiding numerical simulations of such systems.

Key words: accretion, accretion discs – MHD – stars: formation – ISM: jets and outflows.

1 INTRODUCTION

A common feature of protostellar accretion discs is their association with collimated, energetic outflows (e.g. Cabrit 2007). These outflows are widely believed to represent centrifugally driven winds that are launched along large-scale, ordered magnetic fields (e.g. Königl & Pudritz 2000; Pudritz et al. 2007). Such winds could in principle be efficient transporters of disc angular momentum (e.g. Blandford & Payne 1982, hereafter BP82), and it has in fact been argued that there is already observational evidence in several protostellar systems that an outflow of this type carries the bulk of the excess angular momentum from at least some part of the associated accretion disc (e.g. Ray et al. 2007). Protostellar discs are typically weakly ionized, and a certain minimum degree of ionization is required to attain the level of coupling between the matter and the field that enables the vertical magnetic angular-momentum transport mechanism to operate. [A similar requirement must be satisfied also to enable radial angular-momentum transport by a small-scale, turbulent magnetic field; such turbulence could be induced, for example, by the magnetorotational instability (MRI; e.g. Balbus & Hawley 1998).] The inherent magnetic diffusivity tends to counter

*E-mail: raquel@mso.anu.edu.au

the effects of shearing and advection by the differentially rotating accretion flow and therefore makes it possible for the discs to attain a steady state, at least on the dynamical (rotation) time.

The behaviour of a weakly ionized gas can be characterized according to the nature of the dominant diffusivity mechanism for the given density and ionization state: ambipolar, Hall or Ohm (e.g. König & Salmeron 2011). The ambipolar regime, in which the magnetic field lines are effectively frozen into the ions and drift with them relative to the dominant neutral component, can be expected to dominate over the entire disc cross-section in the outermost regions of the disc (at radii $r \gtrsim 10\,\mathrm{au}$) and near the disc surfaces at smaller radii. In the Hall regime the magnetic field is frozen into the electrons and drifts with them relative to the ions and neutrals; this regime could dominate over most of the disc cross-sections on scales $r \sim 1$–$10\,\mathrm{au}$. The Ohm regime, in which the field lines completely decouple from the charge carriers, could potentially dominate near the disc mid-plane on scales ~ 0.1–$1\,\mathrm{au}$ (at smaller radii the mid-plane region likely becomes collisionally ionized). However, as wind-driving discs typically have comparatively lower column densities and mid-plane densities because of their high angular momentum transport efficiency (which results in relatively high inflow speeds), the low-ionization Ohm regime might be curtailed (or even entirely eliminated) in such systems. Even if this were to happen, the Hall-dominated zone would be unlikely to extend to much smaller radii than estimated above on account of the fact that, at sufficiently large densities, the dominant charge carriers become positively and negatively charged grains of equal mass (e.g. Nishi, Nakano & Umebayashi 1991), so that no Hall current can flow.

The structure of radially localized wind-driving protostellar discs in the ambipolar diffusion-dominated regime was investigated by Wardle & König (1993, hereafter WK93). They derived exact solutions that were matched to global, radially self-similar disc–wind solutions of the type introduced by BP82. They analysed the disc solutions by using the hydrostatic approximation, in which the vertical velocity component is neglected inside the disc, and obtained useful algebraic relations that led to a set of parameter constraints on physically viable configurations (see also König 1997). This analysis was generalized by König, Salmeron & Wardle (2010, hereafter Paper I) to the Hall and Ohm diffusivity regimes. In particular, they found that all the viable solutions correspond to four sub-regimes in the Hall domain and three in the Ohm domain, with the solutions in each of the identified parameter sectors having distinct physical properties. The main goal of this paper is to derive exact wind-driving disc solutions that can test these predictions and, more generally, the applicability of the hydrostatic approximation to the description of the salient features of such systems. We concentrate on the Hall diffusivity domain, which, according to the discussion above, should be most relevant (together with the ambipolar regime already discussed in WK93) to the study of the weakly ionized regions of wind-driving protostellar discs. In Paper I, we formulated the problem in terms of a conductivity tensor, specified by the values of the Pedersen, Hall and Ohm components, and discussed its correspondence to a multifluid formulation for the case where only two charged species (one positive and one negative) are present. Our parameter constraints were, in fact, derived in the context of the latter approach. In this paper we employ the conductivity-tensor formulation for the characterization of the solutions that we derive, but we again employ the multifluid formulation in the analysis.

This paper is organized as follows. Section 2 summarizes the system of equations that underlies the radially localized disc model and describes the model parameters as well as the boundary conditions on the equations and the method of their numerical integration. Section 3 provides the corresponding description of the global, self-similar wind model and outlines the procedure used to match the disc and wind solutions. Section 4 presents representative solutions for Hall diffusivity-dominated discs in the different parameter-space sub-regimes identified by the hydrostatic analysis in Paper I and compares them with the predictions (summarized in Appendix A) of the analytical treatment. The main findings of the paper are recapitulated in Section 5.

2 RADIALLY LOCALIZED DISC MODELS

2.1 Dimensionless system of equations in z

In section I.3 (where the prefix 'I' hereafter denotes Paper I) we derived the algebraic relations and ordinary differential equations (ODEs) in the vertical cylindrical coordinate z that describe the vertical structure of the disc at any given value of the radial cylindrical radius r. For clarity and ease of reference, we reproduce them below in dimensionless form. They are the equations of motion

$$\frac{\mathrm{d}w_{\mathrm{r}}}{\mathrm{d}\tilde{z}} = \frac{1}{w_z}\left[\frac{a_0^2}{\tilde{\rho}}j_\phi + 2w_\phi\right], \tag{1}$$

$$\frac{\mathrm{d}w_\phi}{\mathrm{d}\tilde{z}} = -\frac{1}{w_z}\left[\frac{a_0^2}{\tilde{\rho}}j_{\mathrm{r}} + \frac{w_{\mathrm{r}}}{2}\right], \tag{2}$$

$$\frac{\mathrm{d}\ln\tilde{\rho}}{\mathrm{d}\tilde{z}} = \frac{1}{1-w_z^2}\left[\frac{a_0^2}{\tilde{\rho}}(j_{\mathrm{r}}b_\phi - j_\phi b_{\mathrm{r}}) - \tilde{z}\right]; \tag{3}$$

the azimuthal component of the induction equation

$$\frac{\mathrm{d}w_{\mathrm{E}r}}{\mathrm{d}\tilde{z}} = -\frac{3}{2}b_{\mathrm{r}}; \tag{4}$$

Ampère's Law

$$\frac{\mathrm{d}b_{\mathrm{r}}}{\mathrm{d}\tilde{z}} = j_\phi, \tag{5}$$

$$\frac{\mathrm{d}b_\phi}{\mathrm{d}\tilde{z}} = -j_{\mathrm{r}}; \tag{6}$$

the relations linking the electric field in the inertial coordinate system and in the frame comoving with the neutrals

$$e'_{\mathrm{r}} = w_{\mathrm{E}r} + w_\phi - w_z b_\phi, \tag{7}$$

$$e'_\phi = -\epsilon_{\mathrm{B}} + w_z b_{\mathrm{r}} - w_{\mathrm{r}} \tag{8}$$

and Ohm's Law

$$j_{\mathrm{r}} = y(\tilde{\sigma}_{\mathrm{O}} - \tilde{\sigma}_{\mathrm{P}})b_{\mathrm{r}} + \frac{\tilde{\sigma}_{\mathrm{H}}}{b}(e'_z b_\phi - e'_\phi) + \tilde{\sigma}_{\mathrm{P}} e'_{\mathrm{r}}, \tag{9}$$

$$j_\phi = y(\tilde{\sigma}_{\mathrm{O}} - \tilde{\sigma}_{\mathrm{P}})b_\phi + \frac{\tilde{\sigma}_{\mathrm{H}}}{b}(e'_{\mathrm{r}} - e'_z b_{\mathrm{r}}) + \tilde{\sigma}_{\mathrm{P}} e'_\phi, \tag{10}$$

$$
\begin{aligned}
e'_z = &\frac{-(e'_{\mathrm{r}}b_{\mathrm{r}} + e'_\phi b_\phi)(\tilde{\sigma}_{\mathrm{O}} - \tilde{\sigma}_{\mathrm{P}})}{(\tilde{\sigma}_{\mathrm{O}} - \tilde{\sigma}_{\mathrm{P}}) + b^2\tilde{\sigma}_{\mathrm{P}}} \\
&+ \frac{\tilde{\sigma}_{\mathrm{H}}b(e'_{\mathrm{r}}b_\phi - e'_\phi b_{\mathrm{r}})}{(\tilde{\sigma}_{\mathrm{O}} - \tilde{\sigma}_{\mathrm{P}}) + b^2\tilde{\sigma}_{\mathrm{P}}},
\end{aligned} \tag{11}
$$

where we have taken j_z to be $\simeq 0$. The following notation has been used in the above expressions:

$$\tilde{z} \equiv \frac{z}{h_{\mathrm{T}}}, \qquad \tilde{\rho} \equiv \frac{\rho(r,z)}{\rho_0(r)}, \tag{12}$$

$$w \equiv \frac{v - v_{\mathrm{K}}\hat{\boldsymbol{\phi}}}{c_{\mathrm{s}}}, \quad w_{\mathrm{E}} \equiv \frac{c E/B_0 + v_{\mathrm{K}}\hat{\boldsymbol{r}}}{c_{\mathrm{s}}}, \quad e' \equiv \frac{c E'}{c_{\mathrm{s}} B_0}, \tag{13}$$

$$\boldsymbol{j} \equiv \frac{4\pi h_{\mathrm{T}} \boldsymbol{J}}{c B_0}, \quad \tilde{\boldsymbol{\sigma}} \equiv \frac{4\pi h_{\mathrm{T}} c_{\mathrm{s}} \boldsymbol{\sigma}}{c^2}, \quad \boldsymbol{b} \equiv \frac{\boldsymbol{B}}{B_0}, \tag{14}$$

where ρ is the gas density, v is the fluid velocity, J is the current density, B is the magnetic field, σ is the conductivity tensor, incorporating the Pedersen, Hall and Ohm components (σ_{P}, σ_{H} and σ_{O}, respectively), and

$$\boldsymbol{E}' = \boldsymbol{E} + \frac{\boldsymbol{v} \times \boldsymbol{B}}{c} \tag{15}$$

is the electric field in the frame of the neutrals, in terms of E, the electric field in the inertial ('laboratory') frame. Also, $y \equiv E' \cdot B/B^2$, v_{K} is the Keplerian speed, c_{s} is the isothermal speed of sound, $h_{\mathrm{T}} = (c_{\mathrm{s}}/v_{\mathrm{K}})r$ is the tidal scaleheight and the subscript '0' denotes the disc mid-plane.

Under the thin-disc approximation, the vertical component of the magnetic field is constant with height; there is therefore no need to solve the vertical component of Ampére's Law. It can also be shown that the azimuthal component of E (or, equivalently, the variable $w_{\mathrm{E}r}$) is constant with height in our model (see section I.3.7). Therefore, the variable $v_{Br} = c E_\phi/B_z$, which represents the radial drift velocity of the poloidal flux surfaces (see section I.3.6) is also constant with height inside the disc.

In addition to the above equations, the following are also included so as to enable the position of the sonic point (subscript 's') and the (normalized) upward mass flux w_{z0} ($= \tilde{\rho}_{\mathrm{s}}$ under the assumptions that $\tilde{\rho} w_z = \mathrm{const}$ and that the disc is vertically isothermal) to be derived self-consistently as part of the solution (see Section 2.4):

$$\frac{\mathrm{d}\tilde{z}_{\mathrm{s}}}{\mathrm{d}\tilde{z}} = 0, \tag{16}$$

$$\frac{\mathrm{d}w_{z0}}{\mathrm{d}\tilde{z}} = 0. \tag{17}$$

2.2 Parameters

The solutions are specified by the parameters enumerated below. Only a brief summary is provided here; the reader is referred to section I.3.13 for further details.

(i) $a_0 \equiv v_{\mathrm{A}0}/c_{\mathrm{s}}$, the mid-plane ratio of the Alfvén speed (based on the uniform vertical field component B_z) to the isothermal sound speed. It is a measure of the magnetic field strength.

(ii) $c_{\mathrm{s}}/v_{\mathrm{K}} = h_{\mathrm{T}}/r$, the ratio of the tidal scaleheight to the disc radius – a measure of the geometric thinness of the disc. Although this parameter does not appear explicitly in the normalized equations, it is required for matching the disc and wind solutions (see Sections 3.2 and 3.5) and is used to place an upper limit on the mid-plane radial speed in physically viable solutions (see Appendix A).

(iii) The mid-plane ratios of the conductivity-tensor components: $(\sigma_{\mathrm{P}}/\sigma_\perp)_0$ [or $(\sigma_{\mathrm{H}}/\sigma_\perp)_0$] and $(\sigma_\perp/\sigma_{\mathrm{O}})_0$, where $\sigma_\perp = (\sigma_{\mathrm{H}}^2 + \sigma_{\mathrm{P}}^2)^{1/2}$ is the total conductivity perpendicular to the magnetic field. They characterize the conductivity regime of the fluid and are taken here to be independent of z to facilitate the comparison with the analytic results derived in Paper I.

(iv) The mid-plane value of the Elsasser number $\Lambda_0 \equiv v_{\mathrm{A}0}^2/(\Omega_{\mathrm{K}}\eta_{\perp 0})$, where $\eta_{\perp 0} \equiv c^2/4\pi\sigma_{\perp 0}$ is the 'perpendicular' magnetic diffusivity and $\Omega_{\mathrm{K}} = v_{\mathrm{K}}/r$ is the Keplerian angular velocity. This parameter measures the degree of coupling between the neutrals and the magnetic field, with values $\gg 1$ and $\ll 1$ corresponding

to strong and weak coupling, respectively. In this paper we assume (as was done in Paper I) that the disc is everywhere magnetically well coupled, so that Λ_0 is never $\ll 1$. As an alternative to the tensor magnetic diffusivity employed here, one could also write down separate equations for the charged species (see Paper I). Assuming that the charged particles consist only of ions and electrons (denoted by the subscripts 'i' and 'e', respectively), one can write $\Lambda = \Upsilon \beta_{\mathrm{i}}$ in the Hall regime, where Υ is the ratio of the Keplerian rotation time to the neutral-ion momentum exchange time and β_j is the ratio of the gyrofrequency of charged species j to its collision frequency with the neutral gas (see Appendix A). In the ambipolar diffusivity limit (not considered here), $\Lambda = \Upsilon$.

(v) $\epsilon \equiv -v_{r0}/c_{\mathrm{s}}$, the normalized inward radial speed at the mid-plane. This is a free parameter of the *disc solution*, whose value is determined when it is matched to a self-similar global wind solution (see Section 3.5).

(vi) $\epsilon_{\mathrm{B}} \equiv -v_{Br0}/c_{\mathrm{s}} = -c E_{\phi 0}/c_{\mathrm{s}} B_z$, the normalized (vertically constant) azimuthal component of the electric field, which measures the radial drift velocity of the poloidal magnetic field lines through the disc.

2.3 Boundary conditions

The complete system of equations comprises the set of ODEs given by equations (1)–(6), (16) and (17) as well as the algebraic relations (7)–(11). This is a two-point boundary value problem for coupled ODEs. Eight boundary conditions must be formulated, either at the mid-plane or at the critical (sonic) point of the flow, defined as the location where the vertical velocity reaches the isothermal sound speed (or $w_z = 1$). They are applied as follows.

At the mid-plane. We begin by assigning odd symmetry to the radial and azimuthal components of the magnetic field, b_{r} and b_ϕ, which therefore vanish at $\tilde{z} = 0$. Consistently with this choice, the remaining variables (except w_z) have even (reflection) symmetry about the mid-plane and their derivatives vanish at that location. We also adopt $\tilde{\rho} = 1$, which follows directly from the normalization of ρ, and prescribe the radial inwards velocity (measured by the parameter ϵ). The six boundary conditions applied at the mid-plane are thus

$$b_{\mathrm{r}0} = b_{\phi 0} = 0, \tag{18}$$

$$\left(\frac{\mathrm{d}w_{\mathrm{r}}}{\mathrm{d}\tilde{z}}\right)_0 = \left(\frac{\mathrm{d}w_\phi}{\mathrm{d}\tilde{z}}\right)_0 = 0, \tag{19}$$

$$\tilde{\rho}_0 = 1, \qquad -w_{\mathrm{r}0} = \epsilon. \tag{20}$$

Using these boundary conditions and equations (1), (2) and (7)–(10), we arrive at the following expressions for $w_{\phi 0}$ and $w_{\mathrm{E}r0}$:

$$w_{\phi 0} = -\frac{\sigma_{\mathrm{H}0}}{\sigma_{\mathrm{P}0}}\frac{\epsilon}{4} - \frac{a_0^2 \tilde{\sigma}_{\perp 0}^2}{2\sigma_{\mathrm{P}0}}(\epsilon - \epsilon_{\mathrm{B}}), \tag{21}$$

$$w_{\mathrm{E}r0} = \frac{\sigma_{\mathrm{H}0}}{\sigma_{\mathrm{P}0}}(\epsilon - \epsilon_{\mathrm{B}}) + \frac{1}{\sigma_{\mathrm{P}0}}\frac{\epsilon}{2a_0^2} - w_{\phi 0}. \tag{22}$$

At the sonic point. The sonic point is a singular point of equation (3), so an additional boundary condition is obtained by imposing the regularity condition

$$\tilde{z}_{\mathrm{s}} = \frac{a_0^2}{\tilde{\rho}_{\mathrm{s}}}(j_{\mathrm{rs}}b_{\phi \mathrm{s}} - j_{\phi \mathrm{s}}b_{\mathrm{rs}}). \tag{23}$$

Furthermore, the density at $\tilde{z}_{\mathrm{s}}$ is given by

$$\tilde{\rho}_{\mathrm{s}} = w_{z0} \tag{24}$$

(see the discussion just before equation 16). The density derivative at the sonic point can be obtained by differentiating the numerator and denominator of equation (3) (i.e. by applying l'Hôpital's rule), which yields a quadratic equation for $(d\tilde{\rho}/d\tilde{z})_s$. Out of the two roots of this equation, we choose the negative one – corresponding to a positive velocity gradient – as expected for a physical solution.

2.4 Numerical integration of the disc equations

The set of ODEs given by equations (1)–(6), (16) and (17) is integrated using the procedure first outlined in WK93. In brief, we start by assigning the mid-plane values of b_r, b_ϕ, $\tilde{\rho}$, w_r, w_ϕ and w_{Er} (using equations 18 and 20–22), proceed to guess the value of w_{z0} (or, equivalently, $\tilde{\rho}_s$) as well as the position of the sonic point $\tilde{z}_s$, and then integrate from the mid-plane vertically upwards. If the guessed w_{z0} is too high, w_z eventually diverges. If, however, the guessed value is too low, the vertical velocity reaches a maximum and then begins to decrease with $\tilde{z}$. But a vertically decreasing velocity corresponds to a positive density gradient, which is unphysical for an isothermal disc in which the non-thermal forces acting in the vertical direction (namely, the vertical components of gravity and of the Lorentz force) tend to compress the gas. This behaviour of the solutions enables us to bracket the correct value of w_z between two limits. We then improve on the guessed value using bisection until we are close enough to the physical solution to be able to estimate $\tilde{z}_s$ and hence (by extrapolating in $\tilde{z}$) the values of the fluid variables at the sonic point. The boundary conditions given by equations (23) and (24) can then be imposed to obtain the remainder of the disc variables at that location.

To complete the derivation of the full solution, we renormalize z by the estimated height of the sonic point ($\hat{z} \equiv z/z_s$) and integrate the equations simultaneously from the mid-plane ($\hat{z} = 0$) and from the sonic point ($\hat{z}_s = 1$) to an intermediate fitting point (typically $\hat{z} \sim 0.90$) while adjusting the guessed values at both locations iteratively until the solution converges. This procedure is adopted because the integration from the sonic point towards the mid-plane becomes unstable at small values of $\hat{z}$. In carrying out this numerical scheme, it is essential to ensure that w_z attains a value of at least ~0.90–0.95 in the bisection runs before attempting to compute the location of the sonic point and the extrapolated values of the fluid variables there. If this is not done then the estimates of these quantities may not be good enough for the backward integration to the fitting point to be successful.

3 GLOBAL (SELF-SIMILAR) WIND MODELS

The methodology described in Section 2 is appropriate for determining the initial acceleration of the wind from the surfaces of the disc, but it cannot be used to follow the evolution of the outflow on scales where the adopted thin-disc approximation $z/r \ll 1$ breaks down. It is, however, necessary to ensure that the obtained wind solution continues to accelerate and passes through the remaining critical surfaces of the problem, which correspond to the Alfvén and fast-magnetosonic critical points (e.g. BP82; Vlahakis et al. 2000; Ferreira & Casse 2004). Since we cannot self-consistently model this process in view of our radially localized formulation of the disc structure, we approximate a global disc–wind solution by matching the disc solution to a global, radially self-similar (i.e. BP82-type) wind solution. In our cold-wind approximation we only need to impose the regularity condition at the Alfvén critical surface, which allows us to constrain one of the disc parameters (specifically ϵ, which quantifies the mid-plane radial velocity). We

further simplify the treatment by assuming that $\epsilon_B = 0$, which allows us to avoid relating the field-line inclination at the disc surface to the global magnetic flux distribution along the disc (see Ogilvie & Livio 2001). This is essentially the procedure employed (in the ambipolar diffusivity regime) by WK93. In Sections 3.1–3.4 we describe, in turn, the governing equations, parameters, boundary conditions and numerical integration of the self-similar wind solution. The methodology for matching a localized disc solution to a global wind solution is presented in Section 3.5.

3.1 Governing equations

The wind is described by the steady-state, axisymmetric, ideal-MHD equations (e.g. Safier 1993; Königl & Salmeron 2011) that comprise the conservation of mass

$$\nabla \cdot (\rho \boldsymbol{v}) = 0 \tag{25}$$

and momentum

$$\rho \boldsymbol{v} \cdot \nabla \boldsymbol{v} = -\nabla P - \rho \nabla \Phi + \frac{\boldsymbol{J} \times \boldsymbol{B}}{c} \tag{26}$$

for the neutral gas, the induction equation for the topology of the magnetic field

$$\nabla \times (\boldsymbol{v} \times \boldsymbol{B}) = 0 \,, \tag{27}$$

Ampère's Law

$$\boldsymbol{J} = \frac{c}{4\pi} \nabla \times \boldsymbol{B} \tag{28}$$

(where, as customary, we have neglected the displacement current), and the solenoidal condition on the magnetic field ($\nabla \cdot \boldsymbol{B} = 0$). In the above expressions, P is the gas pressure and Φ is the gravitational potential of the central object,

$$\Phi = -\frac{GM}{(r^2 + z^2)^{1/2}} \,, \tag{29}$$

where G is the gravitational constant and M is the mass of the protostar. In ideal-MHD flows, the magnetic field and velocity vectors are parallel in a frame that moves with the angular velocity $\boldsymbol{\Omega}_B$ of the magnetic flux surfaces,

$$\boldsymbol{v} = \frac{k\boldsymbol{B}}{4\pi\rho} + (\boldsymbol{\Omega}_B \times \boldsymbol{r}) \,, \tag{30}$$

where $k/4\pi$ is the *mass load function* of the wind (the ratio of the constant mass flux to the constant magnetic flux). In the poloidal ($r - z$) plane (subscript 'p'), this equation reduces to

$$\boldsymbol{v}_p = \frac{k\boldsymbol{B}_p}{4\pi\rho} \,. \tag{31}$$

The variables Ω_B and k satisfy $(\boldsymbol{B} \cdot \nabla) \Omega_B = (\boldsymbol{B} \cdot \nabla) k = 0$, and thus are constant along the magnetic field lines (or, equivalently, the wind flowlines). Additional quantities that remain constant along the flow are the specific energy

$$e = \frac{1}{2} v^2 + h + \Phi - \frac{\Omega_B r B_\phi}{k} \,, \tag{32}$$

where h is the enthalpy per unit mass, and the specific angular momentum

$$l = r v_\phi - \frac{r B_\phi}{k} \,, \tag{33}$$

which incorporates the contributions of both the matter (the first term on the right-hand side) and the magnetic field (the second

term). The quantities k, e and l can be expressed in dimensionless form as

$$\kappa \equiv k \, (1 + \xi_b'^2)^{1/2} \, \frac{v_{Kb}}{B_b} \, , \tag{34}$$

$$\varepsilon \equiv \frac{e}{v_{Kb}^2} \tag{35}$$

and

$$\lambda \equiv \frac{l}{\sqrt{GMr_b}} \, , \tag{36}$$

where the subscript 'b' denotes the location of the base of the wind.

We now introduce the self-similarity scalings using the notation of BP82:

$$r = r_b \xi(\chi) \, , \tag{37}$$

$$z = r_b \chi \, , \tag{38}$$

$$v_r = \xi'(\chi) f(\chi) v_{Kb} \, , \tag{39}$$

$$v_\phi = g(\chi) v_{Kb} \, , \tag{40}$$

$$v_z = f(\chi) v_{Kb} \, . \tag{41}$$

In these expressions, $\xi' \equiv \tan\varphi = B_r/B_z$ is the inclination of the field lines with respect to the rotation axis of the star and disc. At the base of the wind, we take $\chi_b = 0$, $\xi_b = 1$, $g_b = 1$ and $f_b = 0$, so the fluid velocity at the launching point of the outflow is exactly Keplerian.

We now sketch the procedure followed by BP82 to obtain the set of ODEs in χ that describes the self-similar wind solution. First, from the scalings (39)–(41), we deduce

$$v^2 = \frac{GM}{r_b}[f^2 U + g^2] \, , \tag{42}$$

where

$$U \equiv 1 + \xi'^2 \, , \tag{43}$$

with the prime indicating a derivative with respect to χ. Similarly, the gravitational potential can be expressed as

$$\Phi = -\frac{GM}{r_b} S \, , \tag{44}$$

where the quantity S is defined by

$$S \equiv (\xi^2 + \chi^2)^{-1/2} \, . \tag{45}$$

Furthermore, since we restrict our analysis to 'cold' solutions, the enthalpy term in equation (32) can be neglected in comparison with the other terms. Substituting equations (32), (33), (42) and (44) into equations (35) and (36) yields

$$\varepsilon - \lambda = \frac{1}{2}(f^2 U + g^2 - 2\xi g) - S = -\frac{3}{2} \, , \tag{46}$$

where we used $\Omega_B = (GM/r_b^3)^{1/2}$. The numerical value on the right-hand side of equation (46) is obtained by evaluating this expression at the disc surface; it remains constant along the flow.

To make further progress, one can use equation (30) to write

$$g = \frac{v_\phi}{(GM/r_b)^{1/2}} = \frac{k}{4\pi\rho} \frac{B_\phi}{(GM/r_b)^{1/2}} + \xi \, , \tag{47}$$

which, together with equation (33), gives

$$B_\phi = \sqrt{\frac{GM}{r_b}} k \left[g - \frac{\lambda}{\xi} \right] \, . \tag{48}$$

Then, substituting equation (48) into equation (47), one obtains

$$g = \frac{\xi^2 - m\lambda}{\xi(1 - m)} \, , \tag{49}$$

where m is the square of the Alfvén Mach number (the ratio of the poloidal speed to the poloidal Alfvén speed). Finally, substituting equation (49) into equation (46) and using $\varepsilon - \lambda = -3/2$, one finds

$$T_w - f^2 U = \left[\frac{(\lambda - \xi^2)m}{\xi(1 - m)} \right]^2 \, , \tag{50}$$

where

$$T_w \equiv \xi^2 + 2S - 3 \, . \tag{51}$$

Note that the gravitational plus centrifugal potential at the position $\{\xi, \chi\}$ can be expressed as $-(GM/r_b)(\xi^2/2 + S)$, which becomes $-(3/2)GM/r_b$ at the base of the wind. It is thus seen that $-T_w/2$ is the gravitational plus centrifugal potential difference (in units of GM/r_b) between the point $\{\xi, \chi\}$ along a flowline and the base of the flow at $\{\xi = 1, \chi = 0\}$, so that T_w must be $\geqslant 0$ for physical solutions.

One can obtain an expression for $dm/dx \equiv \chi_A m'$ (where $x \equiv \chi/\chi_A$ is the vertical coordinate along a flowline in units of the height of the Alfvén point, subscript 'A') by substituting Ampère's Law (equation 28) into the momentum equation (26) and then combining the vertical component of equation (26) (with the thermal pressure term neglected in view of the 'cold flow' approximation) with the differential form of equation (50). The result, presented by BP82, is

$$\frac{dm}{dx} = \chi_A \frac{mS^2 \left[B_1 - B_2(m - 1) - B_3(m - 1)^2 \right]}{\xi T_w (m - 1)(t_w - 1)} \, , \tag{52}$$

where

$$m \equiv \frac{4\pi\rho \left(v_r^2 + v_z^2 \right)}{B_r^2 + B_z^2} = \kappa \xi f J_w \, , \tag{53}$$

$$B_1 \equiv 2m^2 \chi(\xi^2 - \lambda)J_w \, , \tag{54}$$

$$B_2 \equiv \xi(\chi + \xi\xi') \left[(5/4)T_w + \xi^2 - S \right] \, , \tag{55}$$

$$B_3 \equiv J_w \left[\chi(\xi^2 + T_w) - f^2(\chi + \xi\xi') \right] \, , \tag{56}$$

$$J_w \equiv \xi - \chi\xi' \tag{57}$$

and

$$t_w \equiv \frac{1}{T_w} \kappa \xi f^3 J_w^3 S^2 = \frac{m^3}{T_w} \left(\frac{S}{\kappa\xi} \right)^2 \, . \tag{58}$$

We will also make use of

$$\frac{d\xi}{dx} = \chi_A \xi' \, . \tag{59}$$

Equation (52) has two singular points. One of them ($m = 1$) corresponds to the Alfvén critical surface, which occurs at the location ($\chi = \chi_A$ or $x = 1$) where the poloidal velocity component (v_p) becomes equal to the poloidal component of the Alfvén velocity (v_{Ap}). The other singular point ($t_w = 1$) occurs at the location where v_p becomes equal to the fast-magnetosonic speed and corresponds to the so-called *modified* fast-magnetosonic critical surface (e.g. Bogovalov 1994). Although an outflow solution that is fully causally disconnected from the source must cross both of these critical surfaces (e.g. Vlahakis et al. 2000), the condition t_w is not expected to provide any additional constraint on our cold outflow solutions (see Ferreira & Casse 2004) and we therefore ignore it in this work.

Equations (52) and (59) can be integrated from the Alfvén point to the base of the wind to obtain the wind solution. As the location of the Alfvén critical point (χ_A) and the inclination of the field lines at the base of the wind (ξ'_b) are not known a priori, we introduce the additional equations

$$\frac{d\chi_A}{dx} = 0 \tag{60}$$

and

$$\frac{d\xi'_b}{dx} = 0, \tag{61}$$

so that these quantities can be found self-consistently when the equations are integrated.

3.2 Parameters

The global, self-similar wind solutions are specified by the following parameters:

(i) the normalized mass-to-magnetic flux ratio,

$$\kappa = \frac{\tilde\rho_s}{a_0^2} \frac{v_{Kb}}{c_s}; \tag{62}$$

(ii) the normalized total specific angular momentum,

$$\lambda = 1 - \frac{a_0^2}{\tilde\rho_s} \frac{c_s}{v_{Kb}} b_{\phi b}; \tag{63}$$

(iii) the inclination of the field lines at the disc surface, measured by the angle φ that the lines make with the vertical,

$$\xi_b' = b_{rb} \tag{64}$$

(See Section 3.1) Equations (62)–(64) show how the global wind parameters can be represented in terms of the local disc parameters at the base of the wind (see Section 2.2). Note that $\kappa(\lambda - 1) = |b_{\phi b}|$ is restricted to a limited range of values for physically viable solutions (see fig. I.2 and WK93). For given choices of two of the above parameters, the third is constrained by the requirement that the solution accelerates past the Alfvén critical surface (see Section 3.5).

3.3 Boundary conditions

The system of equations that describes the wind consists of the set of ODEs given by equations (52) and (59)–(61), together with the algebraic equations (43), (45), (50), (51) and (53)–(58). This is a two-point boundary value problem; four boundary conditions are required, which can be specified either at the Alfvén point or at the base of the outflow. They are applied as follows.

At the Alfvén point. Two boundary conditions are imposed at this location. First, by definition,

$$m_A = 1. \tag{65}$$

This is a singular point of equations (50) and (52). Applying the regularity condition to equation (50) yields

$$\xi_A = \lambda^{\frac{1}{2}}. \tag{66}$$

Note that one can infer from equations (65) and (66) that the numerator of equation (52) vanishes identically at the Alfvén point, so no additional boundary condition is obtained by applying the regularity condition to the latter equation.

Applying l'Hôpital's rule to equations (50) and (52), and using equations (65) and (66), one arrives at the following expressions for m'_A and ξ'_A:

$$m'_A = \frac{2\xi'_A}{\left(T_{wA} - f_A^2 U_A\right)^{1/2}} \tag{67}$$

and

$$C_1 m_A'^2 + C_2 m'_A + C_3 = 0, \tag{68}$$

where

$$C_1 \equiv \xi_A T_{wA}(t_{wA} - 1), \tag{69}$$

$$C_2 \equiv \xi_A S_A^2 (\chi_A + \xi_A \xi'_A) \left[(5/4)T_{wA} + \xi_A^2 - S_A\right] \tag{70}$$

and

$$C_3 \equiv -4S_A^2 \xi_A \xi'_A \chi_A J_{wA}. \tag{71}$$

From equations (67) and (68) one obtains $(dm/dx)_A = \chi_A m'_A$ and $(d\xi/dx)_A = \chi_A \xi'_A$, which can be used to start the integration from the Alfvén point towards the disc.

At the base of the wind. Here, we could, in principle, use the condition $\xi_b = 1$ from the adopted self-similarity scaling (see equation 37). However, the integration becomes unstable close to the disc surface and ξ' typically diverges as $\chi \to 0$. As a result, a Taylor expansion about $\{\xi = 1, \chi = 0\}$ is used to obtain the fluid variables at a small distance ($\delta x \approx 10^{-4}$) above the disc surface. Specifically, we use

$$f_{\delta x} \approx f'_b \delta x + \frac{f''_b}{2}\delta x^2 \tag{72}$$

and

$$\xi_{\delta x} \approx 1 + \xi'_b \delta x + \frac{\xi''_b}{2}\delta x^2, \tag{73}$$

where

$$f'_b = \frac{(3U_b - 4)^{\frac{1}{2}}}{\left[\kappa^2(\lambda - 1)^2 + U_b\right]^{\frac{1}{2}}}, \tag{74}$$

$$f''_b = \frac{-9\kappa \xi_b'^2 - \frac{1}{4}(3D_1 + 5U_b)\xi'_b f'_b + D_2}{3U_b - 4}, \tag{75}$$

$$\xi''_b = -1 - \frac{U_b}{4} + \kappa\left(1 - 3/f_b'^2\right)\xi'_b f'_b - \frac{D_1}{4}, \tag{76}$$

$$D_1 \equiv \kappa^2(\lambda - 9)(\lambda - 1), \tag{77}$$

$$D_2 \equiv \kappa(3U_b - 1)f_b'^2 + 2\xi'_b f_b'^3 + 2\kappa f_b'^4 \tag{78}$$

and $U_b = 1 + \xi_b'^2$ (see BP82). The two boundary conditions applied at $x = \delta x$ are then

$$f(\delta x) = f_{\delta x} \tag{79}$$

and

$$\xi(\delta x) = \xi_{\delta x}, \tag{80}$$

where the expressions on the left-hand sides of equations (79) and (80) are obtained through the integration of the system of ODEs from the Alfvén point towards the disc and those on the right-hand sides are evaluated using equations (72) and (73).
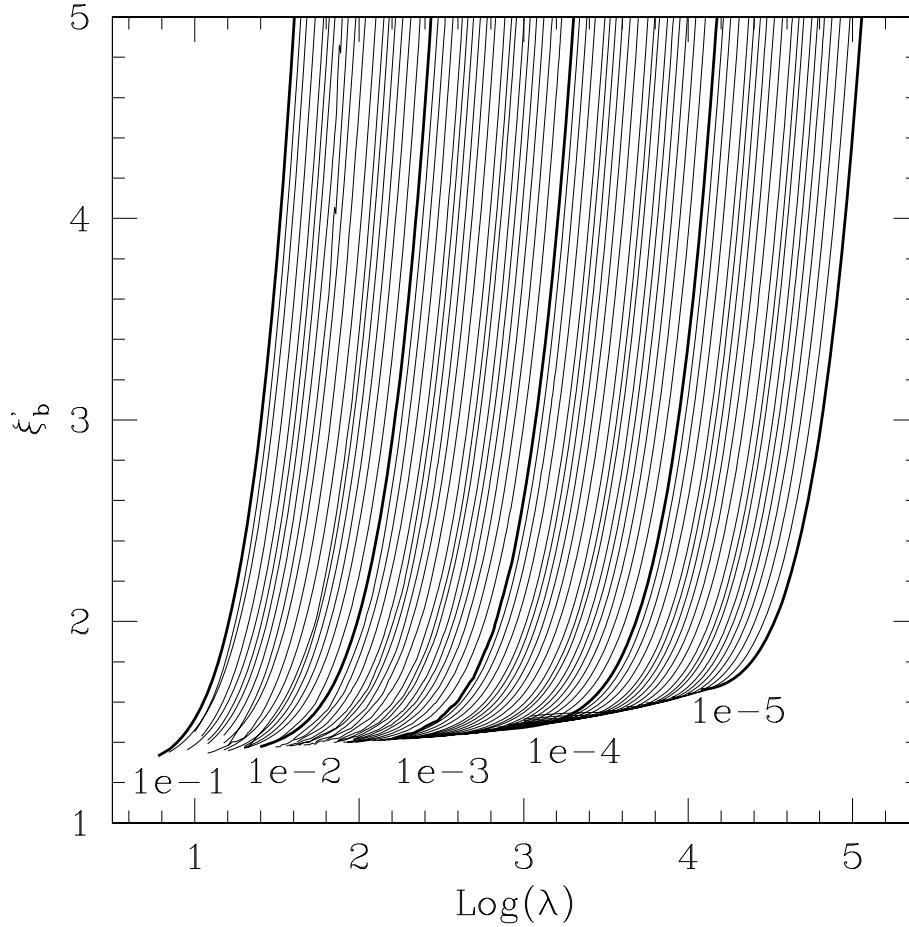
Figure 1. Global, self-similar (BP82-type) wind solutions in parameter space. Solutions are plotted in the $\xi_b'(= b_{rb}) - \log \lambda$ plane, where λ is the normalized total specific angular momentum (including the matter and magnetic field contributions) and ξ_b' measures the inclination of the field lines at the base of the wind. The curves are labelled by the normalized mass-to-magnetic flux ratio, κ: the values of κ that correspond to the darker curves are indicated in the figure. The waviness exhibited by some curves near the lower left corner of the plot is a numerical artefact that reflects the difficulty of computing solutions in the {high-κ, low-λ} region of parameter space. These solutions are available in tabular form as Supporting Information for this article and via the VizieR data base of astronomical catalogues (http://cdsarc.u-strasbg.fr/). A table extract is provided in Appendix B.

3.4 Integration of the wind equations

To integrate the wind equations, it is first necessary to choose the values of the free parameters κ and λ and supply initial (guessed) values of χ_A and ξ_b'. In the coupled disc–wind solutions considered here, the adopted values of κ and λ – as well as the initial estimate of ξ_b' – are calculated from equations (62)–(64), using the values of the fluid variables at the base of the wind that are obtained at the end of the iterations on the disc solution (see Section 3.5). One can then use equations (67) and (68) to evaluate $(d\xi/dx)_A = \chi_A \xi_A'$ and $(dm/dx)_A = \chi_A m_A'$ and start the integration of equations (52) and (59) from the Alfvén point ($x_A = 1$) towards the base of the wind.

Below the Alfvén point (i.e. for $x < 1$), the value of ξ' on the right-hand side of equation (59) is obtained by substituting U, S, T_w, f and J_w (which are found from equations 43, 45, 51, 53 and 57, respectively), as well as m and ξ (which are found from the integrals of equations 52 and 59) into equation (50). This yields the following quadratic equation for ξ':

$$\left(1 - K_1 \chi_A^2 x^2\right) \xi'^2 + 2\chi_A x K_1 \xi + \left(1 - K_1 \xi^2\right) = 0, \tag{81}$$

where

$$K_1 \equiv \left(\frac{\kappa\xi}{m}\right)^2 \left\{ T_w - \left[\frac{(\lambda - \xi^2)m}{\xi(1 - m)}\right]^2 \right\} . \tag{82}$$

Out of the two possible roots of this equation, we choose the one that satisfies the condition $\tan\varphi \equiv \xi' < \tan\theta \equiv \xi/\chi$, as appropriate for a solution that describes a collimating wind.

As discussed at the end of Section 3.3, the boundary conditions at the disc are actually applied at a small distance δx above the surface, where the values derived by integrating down from the Alfvén surface are matched (via equations 79 and 80) to the values obtained by stepping off the mid-plane with a Taylor expansion. The full solution is then found by iterating on χ_A and ξ_b until convergence is reached. Using this procedure, we derived wind solutions for a wide range of values of the parameters κ and λ (see Fig. 1). This solution 'library' is useful when one proceeds to smoothly match a radially localized disc solution to a global wind solution (see Section 3.5). It is available in tabular form as Supporting Information in the electronic version of this article and on the VizieR data base of astronomical catalogues (http://cdsarc.u-strasbg.fr/).

3.5 Matching the (localized) disc and (global) wind solutions

Having derived a localized disc solution as described in Section 2.4, one calculates the associated parameters of a self-similar wind solution (κ, λ and ξ'_b) using equations (62)–(64). The parameter combination obtained in this way does not, however, generally correspond to a wind solution that crosses the Alfvén critical surface. In the next step, one derives a self-similar wind solution as described in Section 3.4, using the given values of κ and λ and employing the value of ξ'_b from equation (64) as an initial guess in implementing the boundary conditions at the base of the wind. The final value of ξ'_b from the wind iteration will, in general, be different from b_{rb}, so equation (64) will not be satisfied. To obtain a self-consistent disc–wind solution, one iterates on the disc and the wind solutions, using ϵ (the normalized mid-plane radial velocity) as an adjustable parameter, until the value of ξ'_b from the wind iteration satisfies equation (64). The CPU time to compute either a disc or a wind solution as described above is typically no more than a few seconds on a 2.4 GHz, AMD Opteron system. On the other hand, the CPU time associated with obtaining a matched disc–wind solution varies with the particular case, but it is not unusual for the entire procedure to take up to 15–20 min.

4 RESULTS

In this section, we discuss the main features of radially localized solutions of well-coupled, wind-driving discs in the Hall diffusivity domain. In Paper I, we identified four parameter sub-regimes in this domain by imposing general physical constraints on viable solutions in the context of the hydrostatic approximation, wherein the vertical velocity component is neglected. This approximation has made it possible to derive algebraic relations that characterize the extent of each sub-regime and the distinguishing properties of the associated solutions. These are summarized in Tables A1 and A2, respectively, of Appendix A, where we also collect some of the algebraic expressions that were employed in the derivation of these results. In Section 4.1 we present representative solutions for these four sub-regimes (labelled by the Roman numerals 'i' through 'iv') and compare their properties with the predictions of Table A2. We then proceed (Section 4.2) to analyse the dependence of the solutions on the conductivity-component ratio $|\sigma_H|/\sigma_\perp$ as well as on the sign of the Hall conductivity $\tilde{\sigma}_H$ (i.e. on the magnetic field polarity) and on the parameter ϵ. We also test whether physically viable solutions are indeed excluded from the parameter regimes that are 'forbidden' according to the hydrostatic analysis. Finally, in Section 4.3, we present illustrative disc solutions that are matched to self-similar wind solutions and briefly discuss the properties of the joint disc–wind solutions obtained in this way.

In all of our disc models we set the parameter ϵ_B to be identically zero. This parameter, which measures the radial drift velocity of the poloidal magnetic field lines (see section I.3.13), depends on the global distribution of B_z along the disc and, therefore, cannot be obtained self-consistently in our localized formulation. The justification for setting $\epsilon_B = 0$ in our analysis is discussed in WK93 and in appendix I.A. Basically, solutions characterized by the same value of the parameter combination ($\epsilon - \epsilon_B$) are qualitatively similar, a property that results from the fact that the only change in the underlying system of equations brought about by switching to a reference frame anchored in the radially drifting poloidal flux surfaces (which move with the radial velocity $v_{Br0} = -\epsilon_B c_s$) is the substitution of $v_r - v_{Br0}$ for the radial velocity v_r in all the equations

except the angular momentum conservation relation, which remains unchanged.

An additional simplification that we employ is to have the Ohm, Pedersen and Hall conductivity terms (σ_O, σ_P and σ_H, respectively) scale with the gas density ρ and magnetic field amplitude B as ρ/B^2. We adopt this dependence since it results in the local matter–field coupling parameter Λ being constant with height. This is convenient for comparison of our solutions with the analytic results of Paper I, which were effectively obtained under the same approximation, as well as with the solutions derived by WK93 in the ambipolar diffusivity regime, where the corresponding value of Λ was similarly assumed not to vary with height. Further calculations, exploring the properties of solutions computed with more realistic ionization and conductivity profiles, will be presented elsewhere.

4.1 Illustrative disc solutions in the Hall parameter sub-regimes

In this subsection, we present representative solutions for the four Hall parameter sub-regimes (see Table 1). We first divide them according to whether the value of the mid-plane Elsasser number Λ_0 is $>1/2$ (Cases i and iii; Fig. 2) or $<1/2$ (Cases ii and iv; Fig. 3), which is one of the two classification criteria that define these sub-regimes.[1] We further divide them according to the second classification criterion, which is whether $s_0 \equiv \beta_{e0}\beta_{i0}$, the mid-plane value of the ion slip factor, is >1 (Cases i and ii, shown in the left-hand panels of Figs 2 and 3, respectively) or <1 (Cases iii and iv, depicted in the corresponding right-hand panels of these figures). The variables β_{i0} and β_{e0} are, respectively, the mid-plane values of the ion and electron Hall parameters (see equation A1). Now, the hydrostatic analysis implies that viable solutions must satisfy $s_0 > 1$ in the ambipolar diffusivity regime (WK93) and $s_0 < 1$ in the Ohm diffusivity regime (Paper I). One can therefore classify Cases (i) and (ii) as being in the 'ambipolar diffusion-modified' Hall regime and Cases (iii) and (iv) as being in the 'Ohm diffusion-modified' Hall regime. This description is supported by the fact that the parameter constraints and solution properties derived for the Hall Case (i) are identical to those in the ambipolar diffusivity limit, with a similar correspondence holding between the Hall sub-regime (iii) and the Ohm sub-regime (i) (see Paper I).

We use the solution for Case (i) (left-hand panel of Fig. 2) as a representative model that illustrates the overall properties of well-coupled wind-driving discs. The top panel of this figure shows the gas density as well as the radial and azimuthal components of the magnetic field as functions of height between the mid-plane and the sonic point. The bottom panel depicts the velocity components. This layout is used also in all the other figures in this paper that depict the vertical structure of the disc solutions.

The representative disc solution exhibits the following overall properties (WK93). In the *quasi-hydrostatic layer* straddling the mid-plane ($0 \lesssim |\tilde{z}| \lesssim 0.4$ in this example), the magnetic field lines are radially bent and azimuthally sheared (see equations 5 and 6), and matter loses angular momentum to the magnetic field. This enables the disc material to flow towards the protostar (i.e. $\epsilon \equiv -w_{r0} > 0$) and results in a radial drag on the ionized disc component (assuming that ϵ_B remains $<\epsilon$; see WK93 and appendix I.A). This drag must be balanced by magnetic tension (see equations 5,

---

[1] Computing solutions for $\Lambda_0 < 1/2$ has proven to be numerically challenging. For this reason, the solutions presented in Fig. 3 correspond to values of Λ_0 that are only slightly smaller than 1/2.

Table 1. Key properties of the solutions shown in Figs 2 and 3. We list the first to third inequalities of Table A1 (representing, respectively, the requirement for a sub-Keplerian flow within the disc, the wind-launching condition and the lower bound on the height of the base of the wind) for each case as well as the mid-plane values of the ion slip factor $s \equiv \beta_e \beta_i$ and of the matter–field coupling parameter $\Lambda \equiv a^2 \tilde{\sigma}_\perp$, which is equal to $\Upsilon |\beta_i|$ in the limit ($|\tilde{\sigma}_H / \tilde{\sigma}_\perp - 1| \ll 1$) (see equation I.95). These parameters form the basis of the classification scheme of viable solutions in the Hall diffusivity regime (see section I.5). The base of the wind and the sonic-surface heights (z_b and z_s, respectively) are in units of both the tidal scaleheight h_T and the actual (magnetically reduced) pressure scaleheight h, where the latter is determined in each case as the value of z where the density drops to $\rho_0 / \sqrt{e}$. The mass accretion rate per disc circumference is evaluated from $\dot{M}_{in} / 2\pi\varpi_0 = -2 \int_0^{z_b} \rho v_r dz$, and the listed value ($\mathcal{M}_{in}$) is this quantity normalized by $\rho_0 c_s h_T$.

Illustrative disc solution	Case (i) Fig. 2 (left)	Case (iii) Fig. 2 (right)	Case (ii) Fig. 3 (left)	Case (iv) Fig. 3 (right)
Constraints	$\frac{1}{\sqrt{2\Upsilon_0}} \lesssim a_0 \lesssim 2 \lesssim \epsilon \Upsilon_0$	$\frac{1}{\sqrt{2\Upsilon_0}} \lesssim a_0 \lesssim 2 \lesssim \epsilon \Upsilon_0 s_0$	$\sqrt{\beta_{i0}} \lesssim a_0 \lesssim 2\sqrt{\Upsilon_0 \beta_{i0}} \lesssim \frac{\epsilon}{2\beta_{i0}}$	$\sqrt{\beta_{i0}} \lesssim a_0 \lesssim 2\sqrt{\Upsilon_0 \beta_{i0}} \lesssim \frac{\epsilon \beta_{e0}}{2}$
	$0.2 \lesssim 1 \lesssim 2 \lesssim 9$	$0.1 \lesssim 1 \lesssim 2 \lesssim 10$	$0.4 \lesssim 0.4 \lesssim 1 \lesssim 3$	$0.3 \lesssim 0.4 \lesssim 1 \lesssim 3$
$s_0 = \beta_{e0} \beta_{i0}$	11	0.2	2.2	0.6
$\Lambda_0 = a_0^2 \tilde{\sigma}_{\perp 0}$	5.0	5.0	0.46	0.46
Properties				
$\tilde{\sigma}_O$	100	10.0	41	20
$\tilde{\sigma}_H$	4.0	4.0	3.0	3.0
$\tilde{\sigma}_P$	3.0	3.0	0.75	0.75
β_{e0}	16	1.6	12.9	6.3
β_{i0}	0.69	0.13	0.17	0.1
Λ_0	5.0	5.0	0.46	0.46
Υ_0	9.1	50	2.8	5.2
a_o	1.0	1.0	0.4	0.4
ϵ	1.0	1.0	1.0	1.0
h/h_T	0.12	0.12	0.16	0.16
z_b/h_T	3.0	3.0	2.3	2.3
z_s/h_T	4.7	4.9	6.0	6.9
z_b/h	25	25	14	14
z_s/h	39	41	37	42
ρ_s/ρ_0	2.1×10^{-10}	2.2×10^{-10}	1.1×10^{-5}	5.9×10^{-6}
$\xi_b' = B_{rb}/B_z$	1.4	1.4	3.3	3.3
$|B_{\phi b}|/B_z$	0.12	0.13	1.2	1.2
$\mathcal{M}_{in}$	0.48	0.48	0.72	0.70

8 and 10), which is consistent with the field lines bending radially outwards. Furthermore, as the magnetic tension also partially supports the fluid against the gravitational pull of the protostar (see equations 1 and 5), the gas motion in this region is sub-Keplerian. Further up but still below the base of the wind (defined as the height $\tilde{z}_b$ where $v_\phi = v_K$ and located in this solution at $z \approx 3.0$) lies the *transition zone* ($0.4 \lesssim |\tilde{z}| \lesssim 3.0$). In this layer the magnetic pressure comes to dominate the thermal pressure because of the strong drop in the gas density away from the mid-plane, and the magnetic field lines are locally straight. Note that everywhere within the disc the radial velocity is negative, the azimuthal velocity is sub-Keplerian and the vertical velocity is subsonic (highly so in the quasi-hydrostatic layer). Finally, as the angular velocity of the magnetic field lines is nearly constant along the poloidal flux surfaces (it is exactly constant only when ϵ_B is identically zero; see Königl 1989), their azimuthal velocity increases with radius until, eventually, they overtake the fluid (whose azimuthal velocity decreases with radius according to the Keplerian rotation law). In the hydrostatic limit ($v_z \to 0$) and with $\epsilon_B = 0$ this occurs at the height $\tilde{z}_b$, and under the same assumptions this is also the location where v_r changes sign.[2] The solution region above $\tilde{z}_b$ (between $\tilde{z}_b \approx 3.0$

[2] In an exact solution, where v_z is >0 near the top of the disc, the heights where $v_\phi = v_K$, $v_\phi = r\Omega_B$ and $v_r = 0$ do not exactly coincide, although typically they remain close to each other.
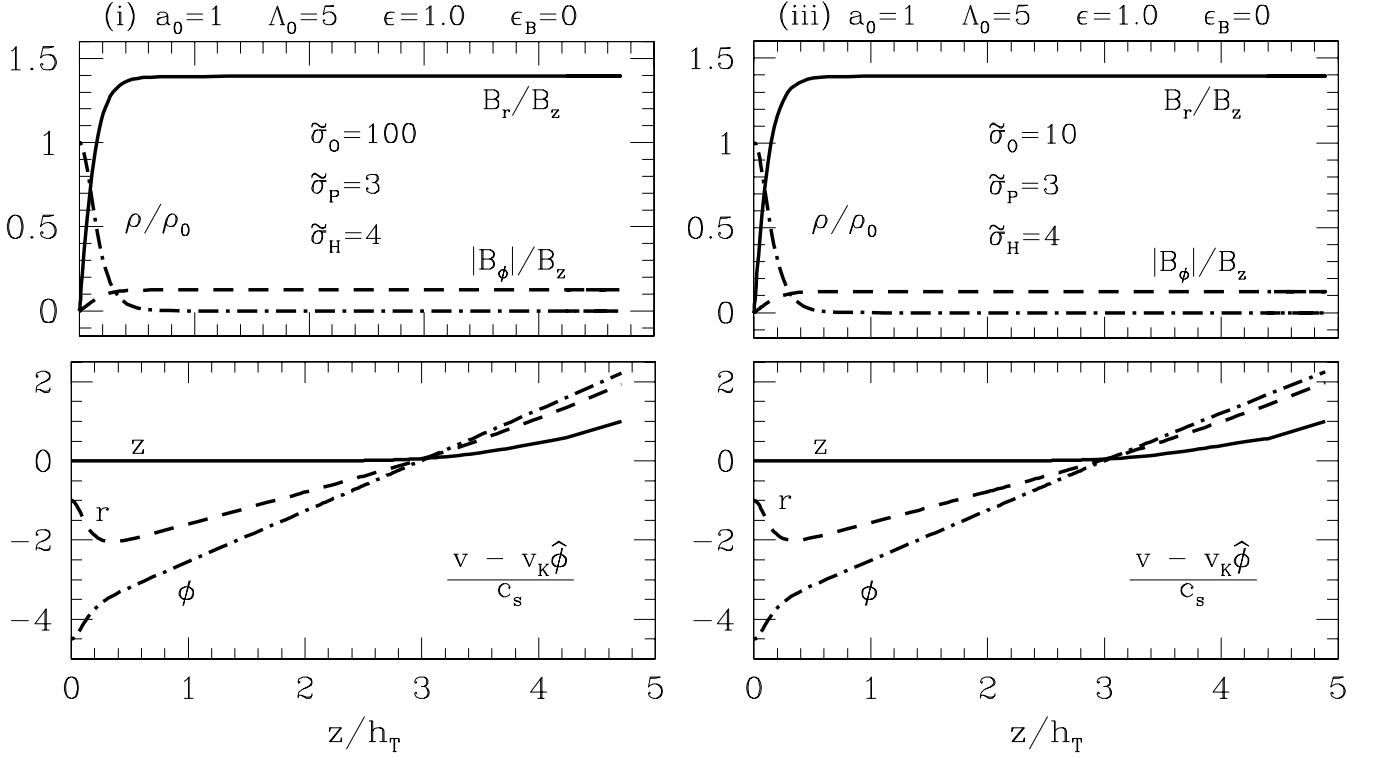
and the sonic surface at $\tilde{z}_s \approx 4.7$) represents the *base of the wind*. In this region v_r is >0, v_ϕ is super-Keplerian and the magnetic field transfers angular momentum back to the matter, causing the uppermost layers of the disc to be driven out centrifugally (with the mass flux in the wind effectively fixed by the regularity condition at sonic critical point of the disc solution).

The distinguishing properties of the four Hall sub-regimes, as inferred in the context of the hydrostatic approximation, are listed in Table A2. To see how the expressions derived in this approximation for $|db_r/db_\phi|_0$, $\tilde{h} \equiv h/h_T$ (where h is the magnetically reduced density scaleheight, defined as the location where the density drops to $\rho_0/\sqrt{e}$) and $\tilde{z}_b/\tilde{h}$ compare with the properties of the full solutions listed in Table 1, we need to relate the parameters β_{i0}, β_{e0} and Υ_0 used in the two-component plasma formulation of Paper I to the tensor conductivity components employed in this work. The parameter Υ_0 is the mid-plane value of the neutral–ion coupling function given by equation (A2) and is equal to the Elsasser number in the ambipolar diffusivity limit. The relationships between these variables and the conductivity ratios can be obtained from equations (I.95)–(I.97) and reduce, in the limit $q \equiv \beta_i/\beta_e \ll 1$, to

$$\Upsilon_0 \approx \Lambda_0 \left(\frac{\tilde{\sigma}_P}{\tilde{\sigma}_\perp} - \frac{\tilde{\sigma}_\perp}{\tilde{\sigma}_O} \right)^{-1}, \tag{83}$$

$$\beta_{i0} \approx \left(\frac{\tilde{\sigma}_P}{\tilde{\sigma}_\perp} - \frac{\tilde{\sigma}_\perp}{\tilde{\sigma}_O} \right) \left(\frac{\tilde{\sigma}_H}{\tilde{\sigma}_\perp} \right)^{-1} \tag{84}$$

Figure 2. Structure of illustrative disc solutions as a function of height above the mid-plane (measured in units of the tidal scaleheight h_T) for the Hall conductivity sub-regimes labelled in Table A1 as Case (i) (left-hand panels) and Case (iii) (right-hand panels) and the model parameters shown in the figure (where all the listed conductivity values pertain to the mid-plane). For these two cases, the matter–field coupling parameter $\Lambda_0 > 1/2$. In both solutions, the top panel shows the gas density (normalized by the mid-plane value) as well as the radial and azimuthal components of the magnetic field (normalized by the vertical component, which is constant with height). The bottom panel depicts the velocity components in a frame rotating at the Keplerian speed, normalized by the isothermal sound speed c_s. The curves terminate at the sonic point. The key properties of both solutions are listed in Table 1.
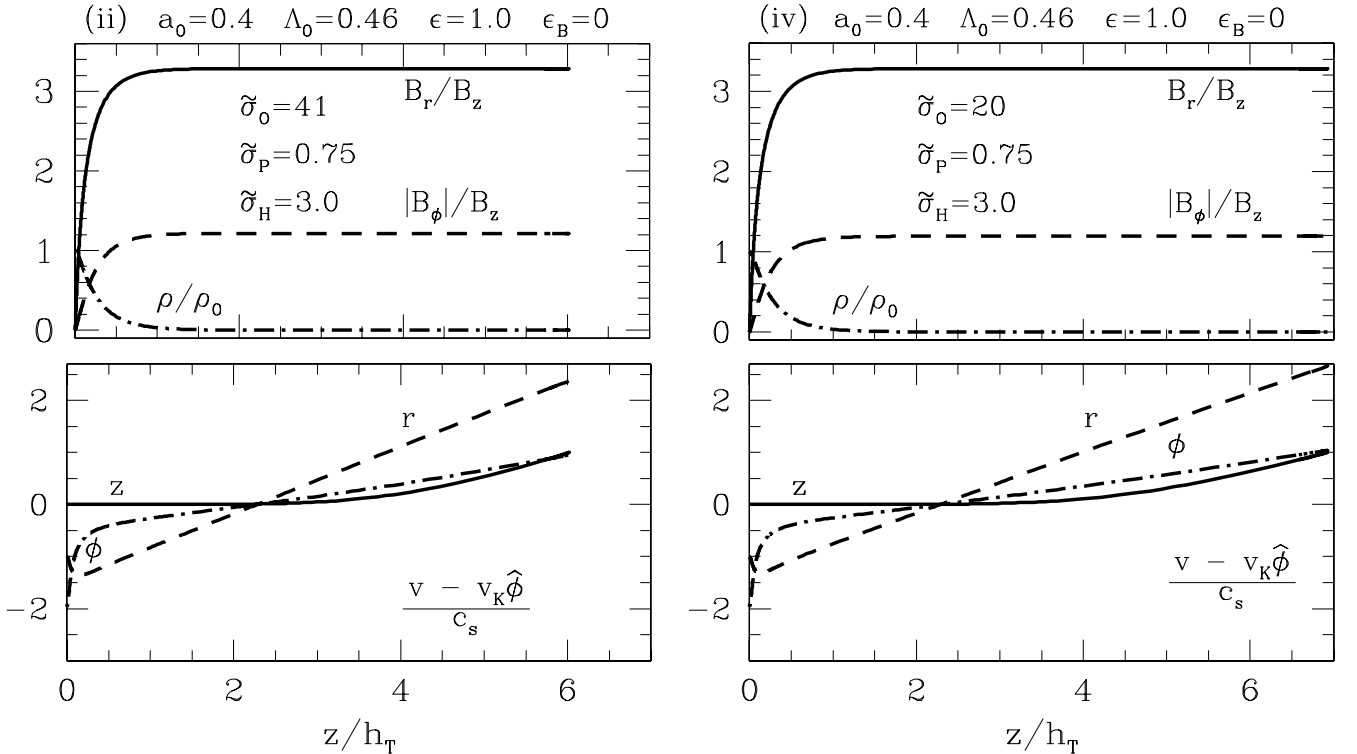
Figure 3. Same as Fig. 2 except that the depicted solutions correspond to Cases (ii) (left-hand panels) and (iv) (right-hand panels) of Table A1, for which $\Lambda_0 < 1/2$. Key properties of these solutions are summarized in Table 1.

and

$$\beta_{e0} \approx \frac{\tilde{\sigma}_H \tilde{\sigma}_O}{\tilde{\sigma}_\perp^2}. \tag{85}$$

4.2 Parameter dependence of the solutions

4.2.1 Dependence on the ratio $|\tilde{\sigma}_H|/\tilde{\sigma}_\perp$

The conductivity ratio $|\tilde{\sigma}_H|/\tilde{\sigma}_\perp$ serves to distinguish the ambipolar diffusivity domain ($\tilde{\sigma}_O \gg \tilde{\sigma}_P \gg |\tilde{\sigma}_H|$) from the Hall diffusivity regime ($\tilde{\sigma}_P \ll |\tilde{\sigma}_H| \ll \tilde{\sigma}_O$): the ambipolar diffusivity limit corresponds to this ratio tending to 0, whereas the Hall limit corresponds to this ratio tending to 1. To illustrate the difference between these two regimes, it may be instructive to compare a solution in the ambipolar diffusivity regime, which satisfies $\Lambda_0 \gtrsim 1$ and $s_0 > 1$ (see Paper I), with a solution in the Hall sub-regime (i), which, as we already noted in Section 4.1, satisfies the same inequalities and, in fact, identical parameter constraints (first line in Table A1). We show such a comparison in Figs 4 and 5. Fig. 4 depicts the vertical run of the density as well as of the transverse magnetic field and the velocity components for two representative solutions in the above-mentioned diffusivity regimes for the same values of the parameters Λ_0, a_0 and ϵ. Fig. 5, in turn, shows the dependence of the
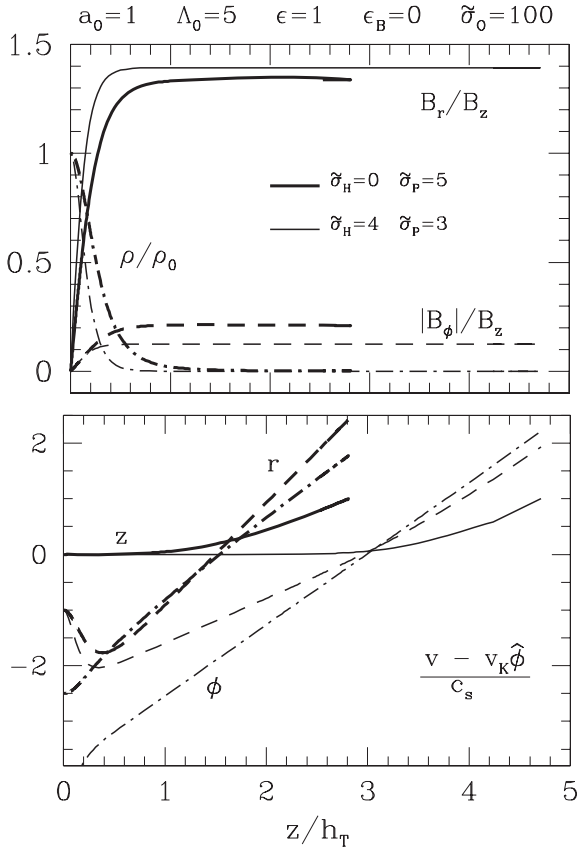

Figure 4. Structure of a wind-driving disc solution as a function of z/h_T for the disc parameters shown in the figure and two different configurations of the conductivity tensor (whose listed components all pertain to the mid-plane). The thick lines correspond to the ambipolar diffusivity limit (for which $\tilde{\sigma}_H = 0$ and $\tilde{\sigma}_O \gg \tilde{\sigma}_P$) and the thin lines to a case where $\tilde{\sigma}_H > \tilde{\sigma}_P$. The normalized upwards mass flux is $\tilde{\rho} w_z = \tilde{\rho}_s = 1.1 \times 10^{-3}$ for the solution in the ambipolar diffusivity limit and 1.4×10^{-6} in the Hall case.
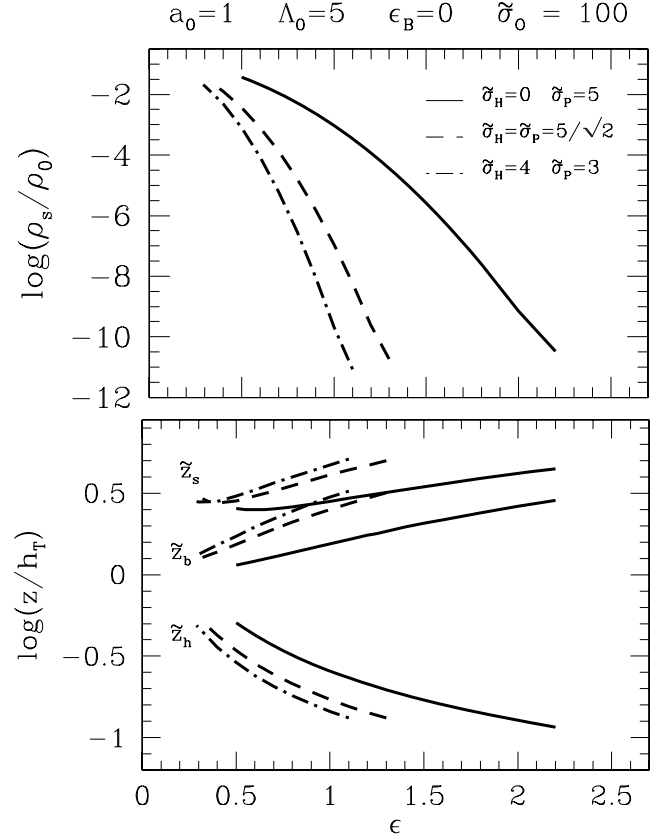

Figure 5. Top panel: density at the sonic point ($\tilde{\rho}_s \equiv \rho_s/\rho_0$) as a function of the normalized inwards velocity at the mid-plane (ϵ) for three configurations of the conductivity tensor characterized by the same values of $\tilde{\sigma}_O$ and $\tilde{\sigma}_\perp$ but different values of the ratio $\tilde{\sigma}_H/\tilde{\sigma}_\perp$. (All the listed conductivities pertain to the mid-plane.) The other model parameters have the same values (indicated in the figure) in each case. Bottom panel: as above, but now plotting the vertical location of the sonic point ($\tilde{z}_s$), the base of the wind ($\tilde{z}_b$) and the magnetically reduced scaleheight ($\tilde{z}_h \equiv \tilde{h}$). In both panels, the solid lines show the ambipolar diffusivity limit ($\tilde{\sigma}_H = 0$), the dashed lines represent the case where $\tilde{\sigma}_H = \tilde{\sigma}_P$ and the dot–dashed lines depict a case where $\tilde{\sigma}_H > \tilde{\sigma}_P$.

density decrement ρ_s/ρ_0 at the sonic surface and of the characteristic heights $\tilde{z}_h \equiv \tilde{h}$, $\tilde{z}_b$ and $\tilde{z}_s$ on the parameter ϵ for the same two choices of the conductivity components (as well as for a solution with an intermediate value of $\tilde{\sigma}_H/\tilde{\sigma}_\perp = 5/\sqrt{2}$) and the same values of Λ_0 and a_0 as in Fig. 4.

The most noticeable differences between the two solutions shown in Fig. 4 are the faster change of the flow variables (corresponding to a smaller value of $\tilde{h}$) and the larger vertical extent of the displayed solution (corresponding to a higher value of $\tilde{z}_s$) in the Hall case. The higher value of $\tilde{z}_s$ implies a lower density at the sonic surface and therefore a lower normalized upwards mass flux ($=\tilde{\rho}_s$) for the Hall solution (see Fig. 5). The decrease (increase) of $\tilde{z}_h$ ($\tilde{z}_s$) with increasing $|\tilde{\sigma}_H|/\tilde{\sigma}_\perp$ when all the other parameter values are held constant is also evident from the curves plotted in Fig. 5. The latter figure further demonstrates that the behaviour of $\tilde{z}_s$ is similar to that of $\tilde{z}_b$, which suggests that $\tilde{z}_b$ could be used as a proxy for $\tilde{z}_s$ in analysing this trend. The parameter dependence of $\tilde{h}$ and $\tilde{z}_b$ can be estimated using the hydrostatic approximation, as discussed in Paper I, and is given by equations (A5) and (A6), respectively. Given that $\Lambda_0 \rightarrow \Upsilon_0 |\beta_{i0}|$ as $|\tilde{\sigma}_H|/\tilde{\sigma}_\perp \rightarrow 1$ and assuming that Λ_0, a_0

and ϵ are held constant, the above equations imply that, to leading order in $|\beta_{i0}|$, $\tilde{h} \propto |\beta_{i0}|$ and $\tilde{z}_b \propto 1/|\beta_{i0}|$ in the ambipolar regime and in the Hall sub-regimes (i) and (ii), for which $s_0 = \beta_{e0}\beta_{i0} \gg 1$. On the other hand, equation (84) implies, given that $\tilde{\sigma}_\perp = \Lambda_0/a_0^2$ (equation I.87) and $\tilde{\sigma}_O$ are fixed, that $|\beta_{i0}|$ *decreases* as $|\tilde{\sigma}_H|/\tilde{\sigma}_\perp$ goes up [and $\tilde{\sigma}_P/\tilde{\sigma}_\perp = (\tilde{\sigma}_\perp^2 - \tilde{\sigma}_H^2)^{1/2}/\tilde{\sigma}_\perp$ goes down]. Taken together, these results explain the manifested dependence of the solutions in Figs 4 and 5 on $|\tilde{\sigma}_H|/\tilde{\sigma}_\perp$.

As a further check on the applicability of the analytical framework developed in Paper I, we note that equations (A5) and (A6) imply a similar dependence of $\tilde{z}_h$ and $\tilde{z}_b$ on $|\tilde{\sigma}_H|/\tilde{\sigma}_\perp$ in the limit $s_0 \ll 1$ (i.e. in the Ohm diffusion-modified Hall regime; Cases iii and iv). In fact, fixing the values of the same parameters as before, these two equations imply that, to leading order in small ratios, $\tilde{h} \propto 1/|\beta_{e0}|$ and $\tilde{z}_b \propto |\beta_{e0}|$ in this case, while equation (85) shows that $|\beta_{e0}|$ *increases* as $|\tilde{\sigma}_H|/\tilde{\sigma}_\perp$ goes up (assuming again that $\tilde{\sigma}_\perp$ and $\tilde{\sigma}_O$ remain unchanged). We have verified that solutions in these regimes indeed exhibit the expected dependence on $|\tilde{\sigma}_H|/\tilde{\sigma}_\perp$.

Yet another test of the predictions of the hydrostatic analysis regarding the dependence of the solutions on $|\tilde{\sigma}_H|/\tilde{\sigma}_\perp$ can be constructed using equation (83) for the parameter Υ_0. As discussed in section I.6 and illustrated in fig. I.2, this analysis indicates that the requirement $\Upsilon_0 \gtrsim 1$ (i.e. that the mid-plane neutral–ion momentum exchange time be shorter than the local orbital time) is a fundamental constraint on viable wind-driving disc models of the type that we consider, and applies to solutions in all the diffusivity regimes (ambipolar, Hall and Ohm). This condition follows directly from the inequalities $\Upsilon_0 |\beta_{i0}| > 1/2$ and $|\beta_{i0}| < 1$ that characterize the Hall Cases (i) and (iii), but, as can be seen by combining the first two parameter constraints reproduced in the first row of Table 1, it can be formally inferred (within the framework of the hydrostatic analysis) to apply also in the other Hall sub-regimes. The illustrative solutions for Cases (ii) and (iv) in Fig. 3 satisfy this inequality, as verified explicitly in Table 1. One can further test the foregoing result in these sub-regimes by holding Λ_0, $\tilde{\sigma}_\perp$ and $\tilde{\sigma}_O$ fixed (as was done above) and decreasing $|\tilde{\sigma}_H|/\tilde{\sigma}_\perp$ (or, equivalently, increasing $\tilde{\sigma}_P/\tilde{\sigma}_\perp$) until (if Λ_0 is sufficiently small) Υ_0 declines to a value <1 where, according to the hydrostatic analysis, viable solutions cease to exist. Such calculations are presented in Fig. 6, where we plot $\tilde{\sigma}_H/\tilde{\sigma}_\perp$ as a function of Υ_0 for representative solutions in these two sub-regimes. It is seen that all viable solutions are indeed restricted to the region $\Upsilon_0 > 1$, validating the above prediction.

4.2.2 Dependence on the field polarity

As was noted in section I.2.1, the Ohm and Pedersen conductivities are always positive, even under a global reversal of the field polarity, since $\tilde{\sigma}_O$ is not a function of the magnetic field strength and $\tilde{\sigma}_P$ only contains magnetic terms that scale as B^2. The Hall conductivity, however, has an overall linear dependence on $B \equiv |\boldsymbol{B}| \, sgn\{B_z\}$ and can thus assume both positive and negative values depending on the direction of the vertical field component. The dependence of $\tilde{\sigma}_H$ on the magnetic field polarity was shown in Paper I to affect both the extent of the parameter ranges where viable wind-driving disc solutions can exist in the Hall domain and the properties of these solutions. We now briefly summarize these results, which were obtained in the hydrostatic approximation assuming an ion–electron plasma.
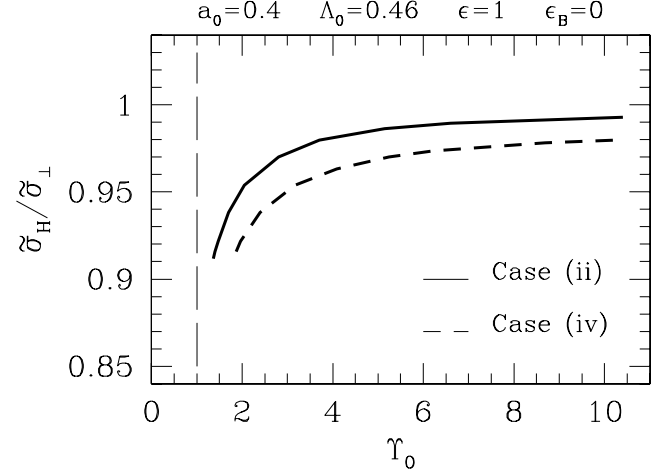

Figure 6. Dependence of the ratio $\tilde{\sigma}_H/\tilde{\sigma}_\perp$ on the parameter Υ_0 for solutions corresponding to the indicated parameter values. The solid and short-dashed curves show solutions for the Hall sub-regimes (ii) (computed with $\tilde{\sigma}_O = 41$ at the mid-plane) and (iv) (computed with $\tilde{\sigma}_O = 20$ at the mid-plane), respectively. In both cases, $\tilde{\sigma}_{\perp 0} = 3.1$. All viable solutions lie to the right of the vertical long-dashed line, where $\Upsilon_0 > 1$, as predicted by the hydrostatic analysis.

The range of values of the parameter $\beta \equiv 1/\beta_{i0}$ for viable solutions was found to be restricted by the following two conditions (see section I.6):

(i) *sub-Keplerian flow below the base of the wind*. This implies that the normalized azimuthal velocity w_ϕ is <0 within the disc, which translates into $db_r/db_\phi < 0$ and $\beta > -2\Upsilon_0$ (equations I.106–I.108).

(ii) *sub-Keplerian azimuthal velocity of the magnetic flux surfaces*, or $w_{\text{Er}0} = -r(\Omega_{B0} - \Omega_K)/c_s > 0$, where $\Omega_{B0} = -cE_{r0}/rB_0$ is the angular velocity of the flux surfaces at the disc mid-plane. This implies (see equation I.113) that either $\beta < -2\Upsilon_0$ or $\beta > -\Upsilon_0/2$ in the Hall domain.

The above two constraints together imply

$$\beta > -\Upsilon_0/2 \qquad \text{in all the Hall sub-regimes}. \tag{86}$$

By combining this inequality with the classification criterion $\Upsilon_0/|\beta| > 1/2$ that distinguishes the Hall sub-regimes (i) and (iii) (see Section 4.1), one obtains

$$-\Upsilon_0/2 < \beta < 2\Upsilon_0 \qquad \text{Cases (i) and (iii)}. \tag{87}$$

Equation (87) predicts that, although there could be both positive- and negative-polarity solutions in the Hall sub-regimes (i) and (iii), no viable solutions should exist in these cases when β decreases below $-\Upsilon_0/2$. This prediction of the hydrostatic analysis is examined in Fig. 7, which plots $\tilde{\rho}_s$, the normalized density at the sonic point, as a function of the coupling parameter Υ_0 for Case (i) solutions derived using the indicated model parameters and corresponding to both positive and negative values of $\beta \propto \tilde{\sigma}_H$ (see equation 84). Since the magnitudes of all the conductivity-tensor components are held constant, all the solutions are characterized by the same absolute value of the ion Hall parameter ($|\beta_{i0}| = 1/1.45$). The figure verifies that viable solutions cease to exist in the region to the left
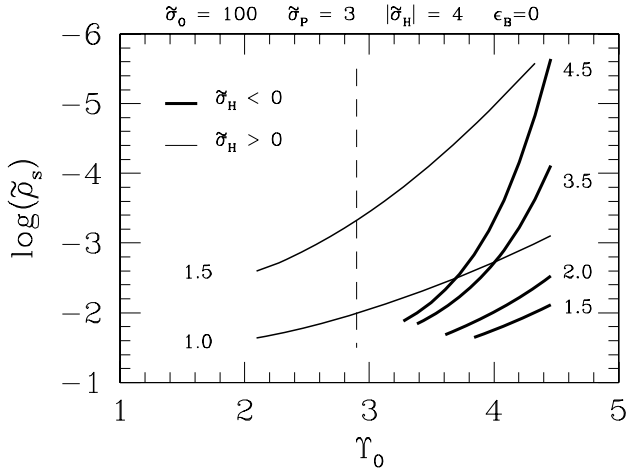
Figure 7. Normalized sonic-point density $\tilde{\rho}_s$ as a function of the parameter Υ_0 for solutions in the Hall sub-regime (i), illustrating the dependence of viable disc models on the magnetic field polarity (i.e. the sign of $\tilde{\sigma}_H$). Curves for $\sigma_H > 0$ are shown by light lines and for $\sigma_H < 0$ by heavy lines, and are labelled by the normalized mid-plane inflow velocity ϵ. (All the listed conductivities pertain to the mid-plane.) The value of $|\beta| \equiv 1/|\beta_{i0}|$ is the same (1.45) for all the solutions. The results are broadly consistent with the prediction of the hydrostatic analysis (equation 87) that there should be no viable solutions for $\tilde{\sigma}_H < 0$ when Υ_0 drops below $2|\beta|$ (i.e. to the left of the vertical dashed line).

of the vertical dashed line, which corresponds to $|\beta| > \Upsilon_0/2$, when $\beta < 0$.[3]

By similarly combining the inequality (86) with the classification criterion $\Upsilon_0/|\beta| < 1/2$ that distinguishes the Hall sub-regimes (ii) and (iv), one obtains

$$\beta > 2\Upsilon_0 \qquad \text{Cases (ii) and (iv)}, \qquad (88)$$

which implies that, for these sub-regimes, self-consistent solutions exist only if the field has a positive polarity. We verified this prediction by adopting the values of a_0, ϵ and $\tilde{\sigma}_\perp$ specified for Cases (ii) and (iv) of Table 1 and changing the value of $\tilde{\sigma}_H/\tilde{\sigma}_\perp$: we found that no negative-polarity solutions could be obtained in these cases.

Even when both positive and negative values of β are allowed, as is the case in sub-regimes (i) and (iii), changing the field polarity modifies the properties of the solutions. This point, which was already made in WK93, is illustrated in Figs 8 and 9, which compare disc solutions that differ only in the sign of $\tilde{\sigma}_H$.[4] The main difference

---

[3] Note that each of the $\beta < 0$ solution curves in Fig. 7 terminates at a finite value of Υ_0 that is lower the higher the value of ϵ. To understand this behaviour, note that, given the parameters that are held fixed in this figure, Υ_0 scales as a_0^2. For a fixed value of a_0, $\tilde{\rho}_s$ increases as ϵ goes down (as seen also in the top panel of Fig. 5). There is a maximum sonic-point density $\tilde{\rho}_s$ that can be attained for the chosen value of a_0, corresponding to the maximum outflow rate for a consistent solution, and this, in turn, determines the magnitude of ϵ for the solution curve that terminates at the given value of a_0. A lower value of a_0 corresponds to a higher lower bound on ϵ because it implies a higher value of $|b_{\phi b}|$ (see equations A3, A4 and 83) and hence a stronger torque on the disc and a correspondingly higher mass accretion rate (reflected in the value of ϵ).

[4] In discussing the differences between Hall-domain solutions with opposite field polarities in section I.6 we explicitly referred to sub-regime (iii), whereas the solutions shown in Figs 8 and 9 correspond to sub-regime (i). It should, however, be clear from the present discussion that the behaviour of solutions in these two sub-regimes is similar in this regard.
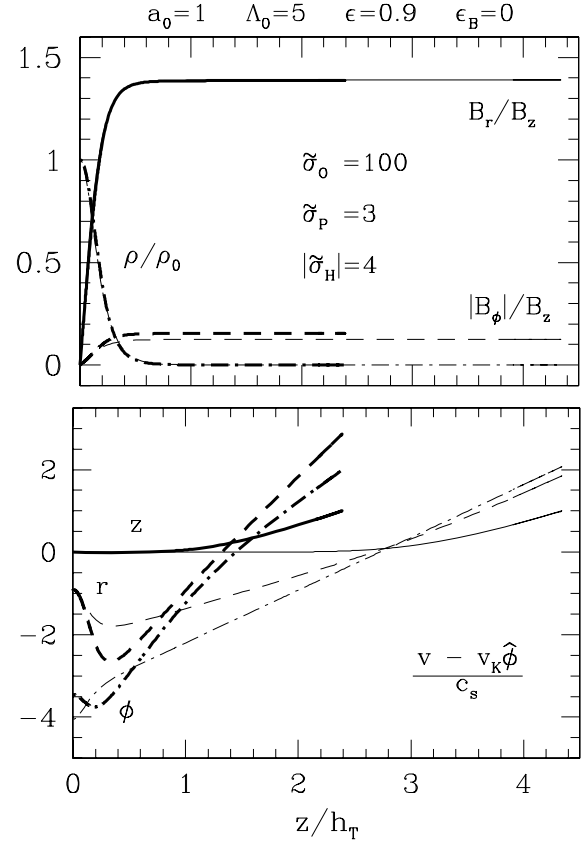

Figure 8. Comparison of two disc solutions that differ only in the sign of the Hall conductivity: $\tilde{\sigma}_H > 0$ for the solution shown by thin lines, and $\tilde{\sigma}_H < 0$ for the solution depicted by thick lines. The normalized upwards mass flux $\tilde{\rho}w_z$ is 9×10^{-9} in the $\tilde{\sigma}_H > 0$ case and 5×10^{-5} in the $\tilde{\sigma}_H < 0$ solution. All the listed conductivities pertain to the mid-plane.

between the two solutions in Fig. 8 is evidently the value of the sonic-point height $\tilde{z}_s$ (corresponding to the termination point of the depicted solution), which is larger ($\simeq 4.3$) in the positive-polarity case than in the negative-polarity solution ($\simeq 2.4$). Fig. 9 confirms this trend: the wind-launching surface ($\tilde{z}_b$) and the sonic surface ($\tilde{z}_s$) are located higher above the mid-plane, and the mass outflow rate (measured by $\tilde{\rho}_s$) is correspondingly lower, in the positive-polarity solutions. The value of $\tilde{z}_h = \tilde{h}$, which represents the scale on which the density and transverse magnetic field components undergo their strongest variation, is also different between the two sets of solutions (it is larger for the negative-polarity model), although this difference is modest in comparison with the change in $\tilde{z}_b$ and $\tilde{z}_s$, and it goes in the opposite direction.

The above behaviour can be understood using the analytic expressions derived in Paper I, and reproduced in Appendix A. Employing the same reasoning as in our analysis of Figs 4 and 5 in Section 4.2.1, we employ the height $\tilde{z}_b$ of the base of the wind as a proxy for $\tilde{z}_s$ in this analysis. Using equations (A5) and (A6), we estimate that, to leading order, $\tilde{h}_+/\tilde{h}_- \approx (2\Upsilon_0 - |\beta|)/(2\Upsilon_0 + |\beta|)$ and $\tilde{z}_{b+}/\tilde{z}_{b-} \approx (\Upsilon_0^2 + 5\Upsilon_0|\beta|/2 + \beta^2)/(\Upsilon_0^2 - 5\Upsilon_0|\beta|/2 + \beta^2)$, where the subscripts '+' and '−' refer to the positive- and negative-polarity cases, respectively. Using also equations (83) and (84), we infer that, for the parameters adopted in Figs 8 and 9, $\tilde{h}_+/\tilde{h}_- \approx 0.85$ and $\tilde{z}_{b+}/\tilde{z}_{b-} \approx 2.28$. These estimates are entirely consistent with the numerical results (for a fixed value of ϵ) shown in the two figures. Furthermore, from equation (A3) we confirm that $|b_{rb}/b_{\phi b}|$ is $\gg 1$ and hence (using equation A4) that $b_{rb} \approx \sqrt{2}/a_0$, independently
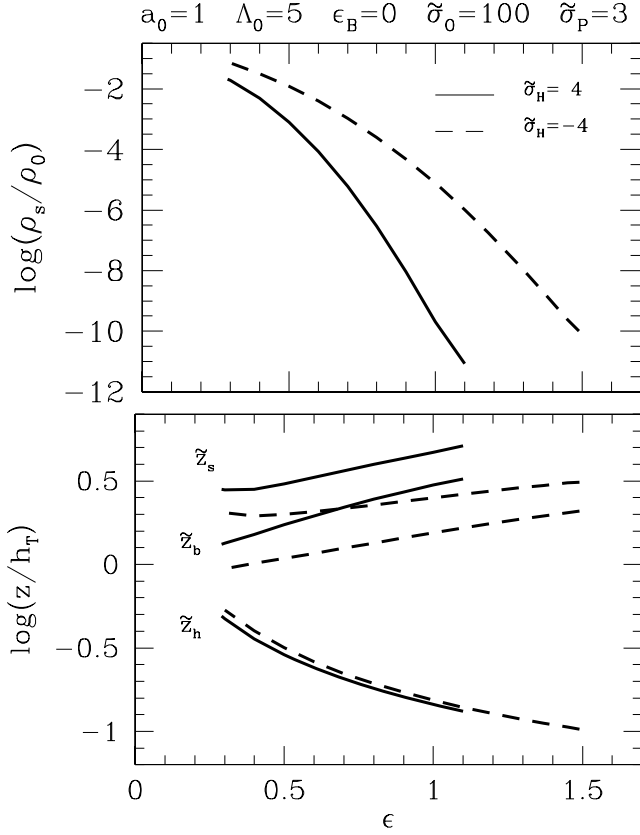
Figure 9. Variation of the normalized sonic-point density (upper panel) and of the characteristic heights $\tilde{z}_s$, $\tilde{z}_b$ and $\tilde{z}_h \equiv \tilde{h}$ (lower panel; cf. Fig. 5) with the model parameter ϵ for the same conductivity-tensor components employed in Fig. 8. The solid lines correspond to $\tilde{\sigma}_H > 0$ and the dashed lines to $\tilde{\sigma}_H < 0$.
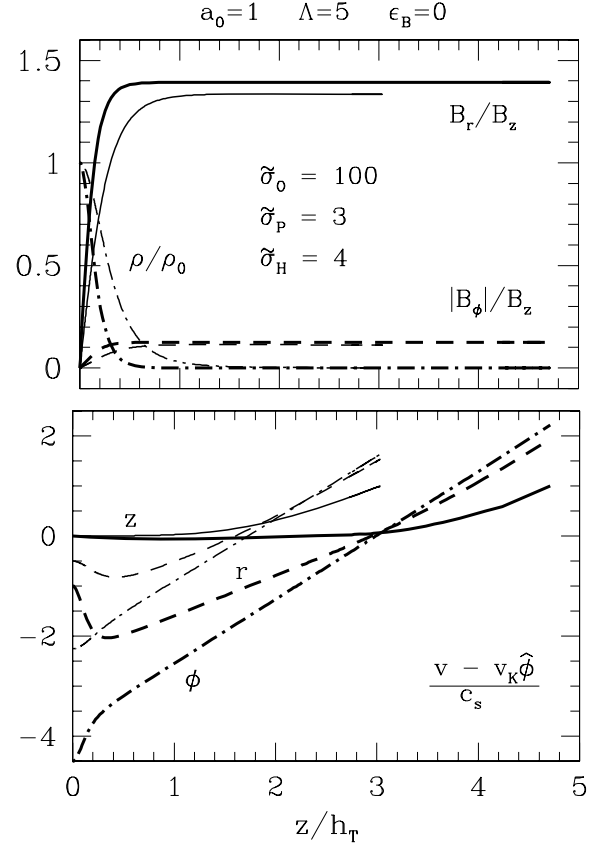
Figure 10. Vertical structure of a wind-driving disc solution for two different values of the radial velocity parameter: $\epsilon = 1$ (thick lines) and $\epsilon = 0.5$ (thin lines). The other model parameters are listed in the figure (with all the conductivity values pertaining to the mid-plane).

of the sign of β, reproducing the actual behaviour of the solutions in Fig. 8. Setting $b_{rb+} \approx b_{rb-}$, we then infer from equations (A3) and (A5) that $b_{\phi b+}/b_{\phi b-} \approx \tilde{h}_+/\tilde{h}_-$ (≈ 0.85 for the adopted parameters). This conclusion, too, is consistent with the result exhibited in Fig. 8.

Although the specific angular momentum at the base of the flow is mostly magnetic (corresponding to the wind model parameter λ being $\gg 1$), the fact that $b_{\phi b+}/b_{\phi b-} < 1$ does not imply that the value of λ is larger in the negative-polarity case. In fact, the converse is true, as can be seen using equation (63), from which it follows that $\lambda_+/\lambda_- \approx (b_{\phi b+}/b_{\phi b-})(\tilde{\rho}_{s-}/\tilde{\rho}_{s+})$. Given that $\tilde{\rho}_{s-}/\tilde{\rho}_{s+}$ is typically $\gg b_{\phi b-}/b_{\phi b+}$ (as the solutions in Fig. 8 demonstrate), we find that $\lambda_+/\lambda_- \gg 1$. Physically, the magnetic torque acting on the disc ($\propto B_z B_\phi$) and correspondingly the mass accretion rate and the rate of inwards angular momentum advection are slightly larger in the negative-polarity case. However, the mass outflow rate is significantly larger in this case and therefore the *specific* angular momentum (the angular momentum per unit mass) has to be much smaller in order for the rate of inwards (radial) and outwards (vertical) angular momentum transport to balance each other. An alternative way of arriving at this conclusion is to consider the wind solutions that are self-consistently matched to these disc solutions. The matched wind solutions lie on a $\xi_b' = $ const curve in the $\kappa - \lambda$ wind parameter space (see equation 64), and along such a curve *higher* values of $\kappa \propto \tilde{\rho}_s$ (see equation 62) correspond to *lower* values of λ (see fig. 2 in BP82).

4.2.3 Dependence on the radial velocity parameter ϵ

To illustrate the dependence on the parameter ϵ (the normalized mid-plane inflow velocity), we plot in Fig. 10 two solutions in the Hall sub-regime (i) that differ only by the value of this parameter. It is seen that, as ϵ decreases from 1.0 (thick lines) to 0.5 (thin lines), the scaleheight $\tilde{h}$ (the scale on which the density and transverse magnetic field components vary most strongly) increases and $\tilde{z}_s$ (the vertical extent of the displayed solution, corresponding to the location of the sonic surface) decreases. These trends are also evident in the solutions depicted in Figs 5 and 9. As we did in Sections 4.2.1 and 4.2.2, we use $\tilde{z}_b$ as a proxy for $\tilde{z}_s$ and employ the hydrostatic-approximation equations (A5) and (A6) to analyse this behaviour. These two expressions show that, with all the other parameters remaining unchanged, $\tilde{h} \propto 1/\epsilon$ and $\tilde{z}_b \propto \epsilon$, which can directly account for the exhibited trends. In both cases, the dependence on ϵ can be traced to the scaling $j_r \propto w_r$ implied by the angular momentum conservation relation (equation 2) in the hydrostatic limit (see section I.4.3).

The hydrostatic analysis presented in Paper I also leads to a lower limit on the value of ϵ, derived from the requirement that the base of the wind be located above a density scaleheight, i.e. $\tilde{z}_b > \tilde{h}$. This implies $\epsilon \Upsilon_0 > (18)^{1/4} \approx 2$ (see Table A2) and represents the third constraint listed in Table A1. To verify the applicability of this condition, we constructed a solution using the same parameters as in the illustrative Case (i) solution depicted in Fig. 2 except that we chose a smaller value of ϵ so that the above constraint is no
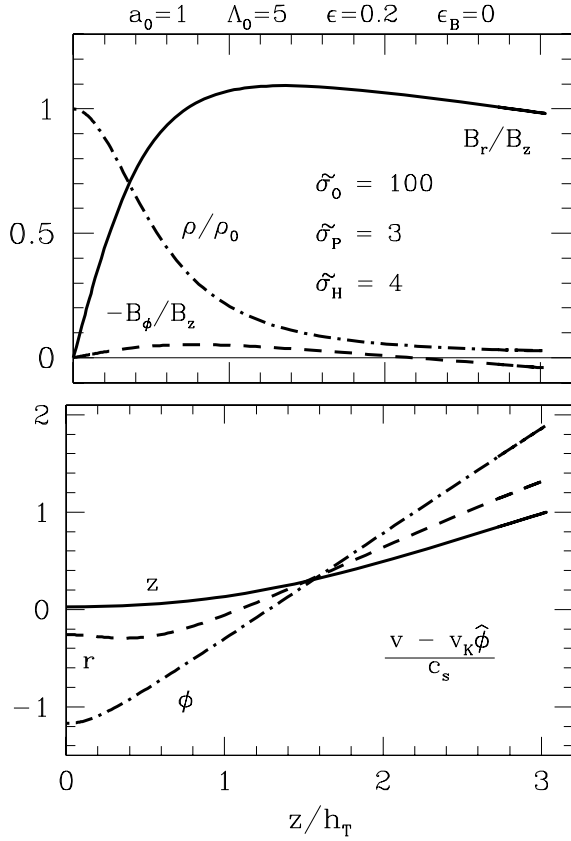
Figure 11. Same as the left-hand side of Fig. 2, but for $\epsilon = 0.2$. In this case $\Upsilon_0 = 9.1$ (see Table 1), so the inequality $\epsilon \Upsilon_0 > 2$ [the third constraint on viable solutions in the Hall sub-regime (i); see the first row in Table 1] is not satisfied. As discussed in the text, the resulting disc solution is unphysical.

longer satisfied. The result, shown in Fig. 11, confirms that, when the above inequality is violated, the solution is no longer physically viable. This is evidenced by the downwards turn of the $|b_\phi|$ and b_r curves above a certain height. A similar solution was presented in fig. 6 of WK93, who explained the origin of this behaviour by noting that, when ϵ decreases to a sufficiently low value, $\tilde{z}_s$ becomes so small and (correspondingly) $\tilde{\rho}_s$ so large that the upwards mass flux carries more angular momentum than is brought in by the accretion flow. Consequently, the gradient of b_ϕ changes sign (with that of b_r following suit) as the magnetic field starts depositing angular momentum back into the flow even before the nominal top of the disc is reached. Such a configuration is likely unstable (e.g. Cao & Spruit 1994).

4.3 Matched disc–wind solutions

The solutions presented in Sections 4.1 and 4.2 have involved the disc model alone. This was done in order to simplify the derivations and was an adequate approach given that we were primarily interested in studying the constraints on the disc model parameters. However, to justify this treatment, it is necessary to demonstrate that matched disc–wind solutions can be obtained for similar disc parameter combinations. This is done in this subsection, where we present two examples of self-consistently matched (local) disc and (global) wind solutions. These solutions correspond to the same values of the parameters Λ_0 and a_0 and of the absolute values of the conductivity-tensor components but have opposite signs of $\tilde{\sigma}_H$: they were obtained using the procedure described in Section 3.5
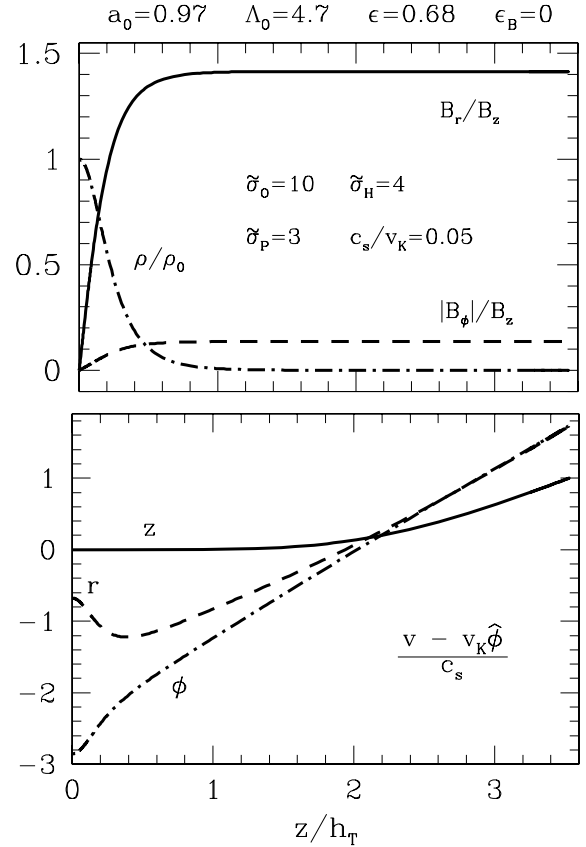

Figure 12. Illustrative disc–wind solution obtained by matching a radially localized disc solution to a global (self-similar) wind solution using the procedure outlined in Section 3.5. The disc model parameters are shown in the figure (with all the conductivity values pertaining to the mid-plane) whereas those of the matched wind solution are $\kappa = 7.9 \times 10^{-4}$, $\lambda = 174$ and $\xi'_b = 1.42$. This solution satisfies the constraints specified in Table A1 for the Hall conductivity sub-regime (iii): $0.1 \lesssim 0.97 \lesssim 2 \lesssim 6.4 \lesssim 10$.

and are shown in Figs 12 (the positive-polarity case) and 13 (the negative-polarity case). As is evident from equations (62) and (63), combining the two solutions requires a specification of the parameter $c_s/v_K = h_T/r$: the above examples were computed for $c_s/v_K = 0.05$.

Our matched solutions correspond to the Hall sub-regime (iii) and are seen to be very similar to the analogous solutions we obtained by considering the disc alone (right-hand panels of Fig. 2). The qualitative differences between the $\tilde{\sigma}_H > 0$ and $\tilde{\sigma}_H < 0$ solutions (essentially a higher value of $\tilde{z}_s$ and lower values of $\tilde{h}$ and of $|b_\phi|$ in the positive-polarity case) are also the same as those found in the 'windless' solution (Figs 8 and 9). This is as expected, since the matching to the wind solution does not affect the physical requirements on a viable disc solution; rather, what it does is fix – through the imposition of the Alfvén regularity condition on the wind solution – the value of one of the disc model parameters that is chosen arbitrarily when the wind solution is not taken into account. In our treatment (see Section 3.5), the disc parameter that is determined in this way is ϵ: it is equal to 0.68 in the $\tilde{\sigma}_H > 0$ solution shown in Fig. 12 and to 0.98 in the $\tilde{\sigma}_H < 0$ solution shown in Fig. 13. In an even more self-consistent solution, the value of the parameter ϵ_B would also be determined by taking into account the conditions outside the disc – in this case the magnetic flux distribution along the disc surface (see section I.3.13) – rather than arbitrarily setting
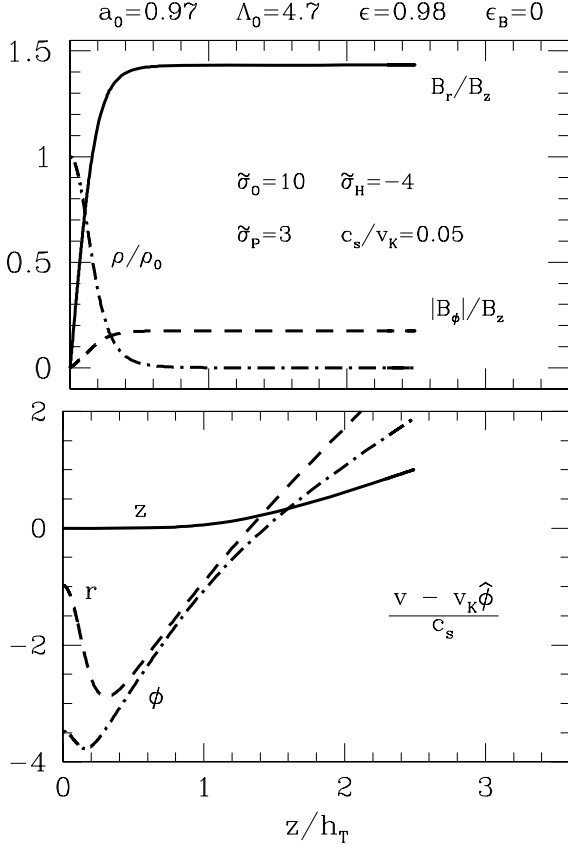
Figure 13. Same as Fig. 12, but with $\tilde{\sigma}_H$ having the opposite sign. All the other disc model parameters except for ϵ, which is determined by imposing the Alfvén regularity condition on the wind solution, are the same as in Fig. 12. In this case the parameters of the matched wind solution are $\kappa = 1.2 \times 10^{-3}$, $\lambda = 144$ and $\xi_b' = 1.43$. This solution, too, satisfies the hydrostatic-analysis constraints for the Hall conductivity sub-regime (iii): $0.1 \lesssim 0.97 \lesssim 2 \lesssim 9.2 \lesssim 10$.

it equal to zero as has been done in this paper and in the analytic derivations of Paper I.[5]

The ratio of the mass outflow rate $\dot{M}_{out}$ in the BP82-type wind to the mass accretion rate $\dot{M}_{in}$ through the disc can be estimated by combining $\dot{M}_{in} \approx 2r^2 B_z^2 |b_{\phi b}|/v_K$ (see equation I.59) and $|b_{\phi b}| = \kappa(\lambda - 1)$ (see Section 3.2) with equation (5.2) in BP82, which gives

$$\frac{\dot{M}_{out}}{\dot{M}_{in}} \approx \frac{\ln{(r_{max}/r_{min})}}{2(\lambda - 1)}, \qquad (89)$$

where r_{max} and r_{min} are, respectively, the outermost and innermost radii of the wind-driving zone. For the solutions shown in Figs 12 and 13, the ratio estimated from equation (89) assuming $r_{max}/r_{min} \approx 10^4$ is ~ 0.03, which is consistent with the values inferred from observations (e.g. Ray et al. 2007).

5 CONCLUSION

In this paper, we continue our study of the viability and properties of weakly ionized protostellar accretion discs that transport their excess angular momentum vertically through the surfaces by means

---

[5] A self-consistent treatment along these lines has, in fact, already been implemented in the fully global self-similar disc/wind model constructed by Teitler (2011).

of centrifugally driven winds. In view of the suggestive evidence that this situation is realized in at least some protostellar systems (e.g. Ray et al. 2007), and yet mindful of the fact that the total radial extent of such wind-driving disc regions is still unknown, we consider radially localized disc configurations (which, however, are joined to a global wind model). We employ the formulation devised by WK93 for modelling steady, geometrically thin, vertically isothermal and nearly Keplerian discs in which magnetic diffusivity counters the shearing and advection of the magnetic field. WK93 assumed that the charge carriers were singly charged ions and electrons and focused on the ambipolar diffusivity regime. In Paper I, we extended this model to the Hall and Ohm diffusivity regimes using the conductivity-tensor formalism, although we reverted to using the multifluid approach employed by WK93 for deriving parameter constraints on physically viable solutions in these regimes. This derivation generalized the corresponding results of WK93 for the ambipolar diffusivity regime and was similarly carried out in the context of the hydrostatic approximation, in which the vertical velocity component is neglected inside the disc (which results in several of the differential equations for the disc structure simplifying to algebraic relations).

The hydrostatic analysis of Paper I indicated that viable wind-driving disc solutions correspond to four parameter sub-regimes in the Hall diffusivity domain and three in the Ohm domain. It also led to analytic estimates of the magnetically reduced (due to magnetic pressure-gradient 'squeezing') density scaleheight and of the location of the disc's surface (where the inflow turns into an outflow), as well as of other pertinent quantities. These results are summarized in Appendix A. In this paper we test these predictions by constructing exact solutions of the disc equations. We concentrate on the Hall regime in view of its expected importance in the inner regions of real systems; we do not consider the low-ionization Ohm regime in this paper given that it may have limited relevance to wind-driving protostellar discs. We characterize the solutions in terms of the conductivity-tensor components (i.e. the Pedersen, Hall and Ohm conductivities). However, to facilitate the comparison with the analytic results of Paper I, which were derived in the framework of the multifluid formulation, we assume that the ratios of these terms are constant with height in the disc and, more specifically, that they scale with the density and field amplitude as ρ/B^2, which implies that the matter–field coupling parameter (the Elsasser number Λ) is also constant with height. We require the derived solutions to cross the sonic critical surface but we do not continue the integration past that surface; this is sufficient for the comparison with the analytic results and greatly simplifies the calculations. However, as recapitulated below, we also demonstrate that these solutions can be matched to wind solutions that extend to large distances (and, in particular, cross the Alfvén critical surface). Our findings can be summarized as follows.

(i) Our numerical solutions are in broad agreement with the parameter constraints obtained under the hydrostatic approximation for the four Hall parameter sub-regimes. In the regions of parameter space that are excluded by the above constraints, wind-driving disc solutions cannot be obtained or are unphysical.

(ii) All viable solutions satisfy the constraint $\Upsilon_0 \gtrsim 1$ (see equation A2). Physically, this condition expresses the requirement that the mid-plane neutral–ion momentum exchange time be shorter than the disc orbital time. As discussed in Paper I, this requirement is predicted to apply in each of the diffusivity regimes and is evidently a fundamental constraint on disc solutions of the type considered here.

(iii) For the same values of a_0, Λ_0 and ϵ (the normalized mid-plane magnetic field amplitude, matter–field coupling strength and radial speed, respectively), increasing the relative contribution of the Hall conductivity (the ratio $|\tilde{\sigma}_H|/\tilde{\sigma}_\perp$) results in a smaller (magnetically reduced) density scaleheight $\tilde{h}$ and in larger heights of the disc and sonic surfaces ($\tilde{z}_b$ and $\tilde{z}_s$, respectively). A higher value of $\tilde{z}_s$ in turn implies a lower density at the sonic surface ($\tilde{\rho}_s$) and hence a lower mass outflow rate.

(iv) The magnetic field polarity affects both the properties of the solutions and the extent of the parameter regimes where viable solutions exist when the Hall current is dynamically important, reflecting the dependence of the Hall conductivity on the sign of B_z. Specifically, we confirmed the following dependence of the solutions on the field polarity (with a positive polarity corresponding to B_z being parallel to the disc rotation vector):

(a) *Hall sub-regimes (i) and (iii).* The parameter β, which is equal to the inverse of the mid-plane ion Hall parameter (equation A1) and thus scales inversely with the *signed* magnetic field amplitude B, is predicted to lie in the range $-\Upsilon_0/2 < \beta < 2\Upsilon_0$. We verified that no solutions exist for $\beta < -\Upsilon_0/2$ and that positive- and negative-polarity solutions have distinct properties. In particular, when the sign of $\tilde{\sigma}_H$ is changed from <0 to >0 and all the other parameter values remain the same, $\tilde{z}_b$ and $\tilde{z}_s$ are increased and the wind outflow rate correspondingly goes down.

(b) *Hall sub-regimes (ii) and (iv).* These parameter regimes are characterized by $\beta > 2\Upsilon_0$. We verified that only positive-polarity solutions can be obtained in this case.

(v) Decreasing the inwards radial speed (ϵ) *increases* the scale over which the fluid variables vary most strongly (the magnetically reduced density scaleheight $\tilde{h}$) but *decreases* both $\tilde{z}_b$ and $\tilde{z}_s$. Furthermore, when the lower limit on the value of ϵ, obtained from the requirement that $\tilde{z}_b > \tilde{h}$ (the third inequality in Table A1) is violated, the computed solutions are found to be unphysical (in that b_r and $|b_\phi|$ start to decrease with $\tilde{z}$ above a certain height).

We also detail the procedure for obtaining global (radially self-similar) 'cold' wind solutions following the methodology introduced by BP82. We compute solutions of this type for a large range of values of the wind model parameters κ, λ and ξ'_b (the normalized mass-to-flux ratio, specific angular momentum and field-line inclination at the disc's surface, respectively). A table of these solutions is available as Supporting Information in the electronic version of this article and on the VizieR data base of astronomical catalogues (http://cdsarc.u-strasbg.fr/). As our radially localized and geometrically thin model cannot be used to follow the propagation of the outflow far from the disc, we match our disc solution to a BP82-type wind solution by adjusting one of the disc model parameters (ϵ) and iterating on the disc and wind calculations until the full solution converges. We present illustrative solutions of this type that demonstrate that matched disc/wind configurations can be obtained for parameter values that are very similar to those of the merely transonic solutions employed in our parameter-space analysis.

The accretion process in protostellar discs may involve a variety of angular-momentum transport mechanisms, including, in particular, radial transport by gravitational torques and by MRI-induced turbulence. In this paper we consider only vertical transport by centrifugally driven winds in an attempt to model a radially localized disc region where this mechanism may dominate. (Note, however, that both vertical transport and radial transport – notably MRI-induced turbulence – could in principle operate at the same disc radius; see Salmeron, Königl & Wardle 2007.) As discussed in Paper I, the large-scale, ordered magnetic field envisioned in this scenario could be either interstellar field advected by the accretion flow or dynamo-generated field produced in either the star or the disc. In view of the strong evidence for strong outflows from the inner regions of protostellar discs, we also neglect alternative modes of angular momentum transport that could be mediated by such a field, including magnetic braking, 'failed' winds and non-steady phenomena. Our treatment has been deliberately simplified to facilitate comparison with the analytic results of Paper I; in particular, we assume that the matter is everywhere well coupled to the field (i.e. $\Lambda > 1$) and that the same conductivity regime applies between the mid-plane and the disc's surface. In reality, the disc may be weakly coupled between the mid-plane and some finite height and its diffusivity properties are expected to change with $\tilde{z}$ (e.g. Salmeron & Wardle 2005). Our approximation should be adequate for representing the behaviour of the dominant diffusivity regime in the well-coupled region of the disc. However, if a significant fraction of the local column density is magnetically weakly coupled then the vertically averaged properties of the disc (such as the inflow speed) could be significantly modified (see Li 1996; Wardle 1997).

In conclusion, the results presented in this paper confirm the validity of the parameter constraints derived in Paper I for physically viable configurations of Hall diffusivity-dominated protostellar discs in which centrifugally driven winds dominate the local angular momentum transport. They also demonstrate that the algebraic expressions derived on the basis of the hydrostatic approximation correctly identify the generic properties of such discs and are useful for clarifying the behaviour of the full numerical solutions. More generally, the theoretical framework developed in WK93, Paper I and the present work can be used to study discs of this type also in other diffusivity regimes and in other astrophysical environments. In particular, it can help interpret observations of such systems by relating the properties of the outflow to those of the underlying disc (e.g. Königl 2010). It may also be useful for guiding non-ideal-MHD numerical simulations of wind-driving discs. One could in principle also combine a succession of localized disc solutions, each matched to a global wind solution, to approximate a radially extended wind-driving disc. This approach might be particularly useful for studying the time evolution of the mass and magnetic flux distributions in such a disc; however, for modelling steady-state configurations, a global self-similarity approach that encompasses both the disc and the wind (e.g. Teitler 2011) would be more accurate.

REFERENCES

Balbus S. A., Hawley J. F., 1998, Rev. Mod. Phys., 70, 1
Blandford R. D., Payne D. G., 1982, MNRAS, 199, 883 (BP82)
Bogovalov S. V., 1994, MNRAS, 270, 721

Cabrit S., 2007, in Ferreira J., Dougados C., Whelan E., eds, LNP Vol. 723, Jets from Young Stars. Springer-Verlag, Berlin, p. 21

Cao X., Spruit H. C., 1994, A&A, 287, 80

Ferreira J., Casse F., 2004, ApJ, 601, L139

Königl A., 1989, ApJ, 342, 208

Königl A., 1997, in Wickramasinghe D. T., Bicknell G. V., Ferrario L., eds, Proc. IAU Colloq. 163, ASP Conf. Ser. Vol. 121, Accretion Phenomena and Related Outflows. Astron. Soc. Pac., San Francisco, p. 551

Königl A., 2010, MNRAS, 407, L79

Königl A., Pudritz R. E., 2000, in Mannings V. G., Boss A. P., Russell S., eds, Protostars & Planets IV. Univ. Arizona Press, Tucson, p. 759

Königl A., Salmeron R., 2011, in Garcia P. J. V., ed, Physical Processes in Circumstellar Disks around Young Stars. Univ. Chicago Press, Chicago, in press (arXiv:1004:1875)

Königl A., Salmeron R., Wardle M., 2010, MNRAS, 401, 479 (Paper I)

Li Z.-Y., 1996, ApJ, 465, 855

Nishi R., Nakano T., Umebayashi T., 1991, ApJ, 368, 181

Ogilvie G. I., Livio M., 2001, ApJ, 553, 158

Pudritz R. E., Ouyed R., Fendt C., Brandenburg A., 2007, in Reipurth B., Jewitt D., Keil K., eds, Protostars and Planets V. Univ. Arizona Press, Tucson, p. 277

Ray T., Dougados C., Bacciotti F., Eislöffel J., Chrysostomou A., 2007, in Reipurth D., Jewitt D., Keil K., eds, Protostars & Planets V. Univ. Arizona Press, Tucson, p. 231

Safier P. N., 1993, ApJ, 408, 115

Salmeron R., Wardle M., 2005, MNRAS, 361, 45

Salmeron R., Königl A., Wardle M., 2007, MNRAS, 375, 177

Teitler S., 2011, ApJ, submitted

Vlahakis N., Tsinganos K., Sauty C., Trussoni E., 2000, MNRAS, 318, 417

Wardle M., 1997, in Wickramasinghe D. T., Bicknell G. V., Ferrario L., eds, Proc. IAU Colloq. 163, ASP Conf. Ser. Vol. 121. Accretion Phenomena and Related Outflows. Astron. Soc. Pac., San Francisco, p. 561

Wardle M., Königl A., 1993, ApJ, 410, 218 (WK93)

APPENDIX A: PARAMETER CONSTRAINTS IN THE HALL LIMIT

The parameter constraints on viable wind-driving disc solutions were obtained in Paper I by applying the hydrostatic approximation to a radially localized disc model under the assumption that the charged component of the weakly ionized disc material consisted of two particle species: positive 'ions' (subscript 'i') and negative 'electrons' (subscript 'e'), each singly charged. Instead of employing two independent ratios of the conductivity-tensor components as model parameters, as is done in this paper, we used the ion and electron Hall parameters, i.e. the ratios of the gyrofrequency and the collision frequency of these two species with the neutrals, which are given by

$$\beta_e = \frac{eB}{m_e c} \frac{1}{\gamma_i \rho} , \qquad \beta_i = \frac{eB}{m_i c} \frac{1}{\gamma_e \rho} \equiv q \beta_e, \qquad \text{(A1)}$$

where c is the speed of light, m is the particle's mass, e is the unit electric charge and the total mass density ρ is used to approximate the neutral mass density. The collisional coupling coefficient γ_j is equal to $\langle \sigma v \rangle_j / (m_j + m)$, where m is the mean mass of the neutral particles and $\langle \sigma v \rangle_j$ is the rate coefficient of momentum exchange of species j with the neutrals. The product $\gamma_i \rho$ ($\gamma_e \rho$) in equation (A1) therefore represents the momentum-exchange collision frequency of the ions (electrons) with the neutrals. In the above definitions, $B \equiv |\mathbf{B}| \, sgn\{B_z\}$, so the sign of the Hall parameter is sensitive to

the magnetic field polarity. It is further assumed that the ions are 'heavy' and the electrons are 'light', so that $q \ll 1$.[6]

Another key parameter employed in Paper I (see also WK93) is

$$\Upsilon \equiv \frac{\gamma_i \rho_i}{\Omega_K} \qquad \text{(A2)}$$

(where ρ_i is the ion mass density), the ratio of the Keplerian rotation time to the neutral–ion momentum exchange time. In the ambipolar diffusivity limit ($\sigma_O \gg \sigma_P \gg |\sigma_H|$ or, equivalently, $|\beta_i| \gg 1$) the Elsasser number Λ (Section 2.2) reduces to Υ, whereas in the Hall diffusivity limit ($\sigma_P \ll |\sigma_H| \ll \sigma_O$ or, equivalently, $|\beta_i| \ll 1 \ll |\beta_e|$) $\Lambda = \Upsilon |\beta_i|$.

The parameter constraints for the four Hall sub-regimes are presented in Table A1, which reproduces table I.1. The physical origin of the imposed constraints is summarized in the caption of this table. The key predicted properties of the solutions in each sub-regime are listed in Table A2, which reproduces table I.2. We also reproduce below some of the expressions used in the derivation of these results that are relevant to the analysis presented in this paper.

The ratio $|db_r/db_\phi|_0$ is given by

$$\left| \frac{db_r}{db_\phi} \right|_0 = \frac{2\Upsilon_0 + \beta}{1 + q\beta^2} \qquad \text{(A3)}$$

(equation I.115), where $\beta \equiv 1/\beta_{i0}$. This expression can be used to approximate $|b_{rb}/b_{\phi b}|$, the ratio of the corresponding magnetic field components at the base of the wind. Another relationship between the field components at $\tilde{z}_b$ is provided by

$$b_{rb}^2 + b_{\phi b}^2 \approx \frac{2}{a_0^2} \qquad \text{(A4)}$$

(equation I.90). Since $|db_\phi/db_r|_0$ is always <1 in the Hall regime, one can approximate, to leading order, $b_{rb} \approx \sqrt{2}/a_0$ and $b_{\phi b} \approx -\sqrt{2}(1 + q\beta^2)/[(2\Upsilon_0 + \beta)a_0]$. The assumption $|db_\phi/db_r|_0 \ll 1$ also leads to the following simplified expression for the magnetically reduced scaleheight:

$$\tilde{h} \approx \frac{2a_0}{\epsilon} \frac{1 + q\beta^2}{2\Upsilon_0 + \beta} \qquad \text{(A5)}$$

(equation I.119). The height of the base of the wind is, in turn, given by

$$\tilde{z}_b \approx \frac{a_0 \epsilon}{3\sqrt{2}\Upsilon_0} \frac{\Upsilon_0^2 + (5/2)\Upsilon_0\beta + \beta^2}{1 + q\beta^2} \qquad \text{(A6)}$$

(see equation I.120). Finally, the Joule dissipation term in Table A2 is evaluated from

$$(\mathbf{j} \cdot \mathbf{e}')_0 = \frac{\epsilon^2}{4\Upsilon_0 a_0^2}(1 + q\beta^2) \left[1 + \left(\frac{2\Upsilon_0 + \beta}{1 + q\beta^2} \right)^2 \right] \qquad \text{(A7)}$$

(see equation I.122). The rate of Joule heating at the disc mid-plane should not exceed the rate of release of gravitational potential energy at that location. This requirement is expressed by the rightmost inequality of Table A1, which involves the ratio of the tidal scaleheight to the disc radius, $h_T/r = c_s/v_K$. This parameter does not

---

[6] In a real disc containing two charged species, the value of q is fixed by the physical properties of the charge carriers (see equations I.7–I.9). This, in turn, constrains the values that the conductivity ratios $\tilde{\sigma}_H/\tilde{\sigma}_\perp$ and $\tilde{\sigma}_\perp/\tilde{\sigma}_O$ can take (see equations 84 and 85). We do not incorporate this constraint into the parameter-space analysis in Section 4 so as not to unduly complicate the discussion; however, we have verified that the 'effective' value of q, obtained from the ratio of equation (84) to equation (85), remains $\ll 1$ for all the solutions that we present.

Table A1. Parameter constraints for wind-driving disc solutions in the limit where the Hall diffusivity dominates and assuming $\epsilon_B = 0$. Four distinct cases can be identified, depending on how the values of $s_0 = \beta_{e0}\beta_{i0}$ and of $2\Lambda_0 = 2\Upsilon_0|\beta_{i0}|$ compare with 1. The first inequality expresses the requirement that the disc remain sub-Keplerian below the wind zone ($\tilde{z} < \tilde{z}_b$), the second is the wind launching condition (the requirement that the magnetic field lines be sufficiently inclined to the vertical for centrifugal acceleration to occur), the third ensures that the base of the wind is located above the (magnetically reduced) density scaleheight and the fourth specifies that the rate of Joule heating at the mid-plane should not exceed the rate of release of gravitational potential energy there.

Case	Limits $s_0 = \beta_{e0}\beta_{i0}$	$\Lambda_0 = \Upsilon_0|\beta_{i0}|$	Parameter constraints – Hall limit (multifluid formulation)						
(i)	>1	>1/2	$(2\Upsilon_0)^{-1/2}$	$\lesssim$	a_0	$\lesssim$	2	$\lesssim$	$\epsilon\Upsilon_0$	$\lesssim$ $v_K/2c_s$
(ii)	>1	<1/2	$\beta_{i0}^{1/2}$	$\lesssim$	a_0	$\lesssim$	$2(\Upsilon_0\beta_{i0})^{1/2}$	$\lesssim$	$\epsilon/2\beta_{i0}$	$\lesssim$ $\Upsilon_0\beta_{i0}v_K/c_s$
(iii)	<1	>1/2	$(2\Upsilon_0)^{-1/2}$	$\lesssim$	a_0	$\lesssim$	2	$\lesssim$	$\epsilon\Upsilon_0\beta_{e0}\beta_{i0}$	$\lesssim$ $v_K/2c_s$
(iv)	<1	<1/2	$\beta_{i0}^{1/2}$	$\lesssim$	a_0	$\lesssim$	$2(\Upsilon_0\beta_{i0})^{1/2}$	$\lesssim$	$\epsilon\beta_{e0}/2$	$\lesssim$ $\Upsilon_0\beta_{i0}v_K/c_s$

Table A2. Key properties of viable disc solutions in the Hall regime. Listed, in order, are the mid-plane values of $|db_r/db_\phi|$, the magnetically reduced scaleheight in units of the tidal scaleheight ($\tilde{h} \equiv h/h_T$), the similarly normalized vertical location of the base of the wind $\tilde{z}_b$ in units of $\tilde{h}$ and the normalized Joule dissipation rate $\boldsymbol{j}\cdot\boldsymbol{e}'$ at the mid-plane.

Case	Limits $s_0 = \beta_{e0}\beta_{i0}$	$\Lambda_0 = \Upsilon_0|\beta_{i0}|$	Solution characteristics – Hall limit $|db_r/db_\phi|_0$	$\tilde{h}$	$\tilde{z}_b/\tilde{h}$	$(\boldsymbol{j}\cdot\boldsymbol{e}')_0$
(i)	>1	>1/2	$2\Upsilon_0$ (>1)	$a_0/\epsilon\Upsilon_0$	$(\epsilon\Upsilon_0)^2/3\sqrt{2}$	$\epsilon^2\Upsilon_0/a_0^2$
(ii)	>1	<1/2	$1/\beta_{i0}$ (>1)	$2a_0\beta_{i0}/\epsilon$	$\epsilon^2/6\sqrt{2}\Upsilon_0\beta_{i0}^3$	$\epsilon^2/4\,\Upsilon_0\,\beta_{i0}^2\,a_0^2$
(iii)	<1	>1/2	$2\Upsilon_0\beta_{e0}\beta_{i0}$ (>1)	$a_0/\epsilon\Upsilon_0\beta_{i0}\beta_{e0}$	$(\epsilon\Upsilon_0\beta_{e0}\beta_{i0})^2/3\sqrt{2}$	$\epsilon^2\,\Upsilon_0\,\beta_{e0}\,\beta_{i0}/a_0^2$
(iv)	<1	<1/2	β_{e0} (>1)	$2a_0/\epsilon\beta_{e0}$	$(\epsilon\beta_{e0})^2/6\sqrt{2}\Upsilon_0\beta_{i0}$	$\epsilon^2\,\beta_{e0}/4\,\Upsilon_0\,\beta_{i0}\,a_0^2$

Table B1. Global, self-similar (BP82-type) wind solutions in tabular form. The solutions are characterized by the values of the parameters κ (the normalized mass-to-magnetic flux ratio), λ (the normalized total specific angular momentum) and ξ_b' (the inclination of the magnetic field lines at the base of the wind), as described in Section 3.2. The normalized height of the Alfvén point (χ_A) is also listed. Only five entries are displayed below; the complete library of tabulated solutions is available as Supporting Information in the electronic version of this paper and via the VizieR data base of astronomical catalogues (http://cdsarc.u-strasbg.fr/). Fig. 1 shows the full range of solutions in graphical form.

κ	λ	ξ_b'	χ_A
1.000×10^{-1}	4.100×10^1	5.092	1.553
1.000×10^{-2}	2.750×10^2	5.018	4.660
1.000×10^{-3}	2.015×10^3	5.006	12.98
1.000×10^{-4}	1.500×10^4	5.013	35.78
1.000×10^{-5}	1.135×10^5	5.001	97.59

APPENDIX B: GLOBAL, SELF-SIMILAR WIND SOLUTIONS IN PARAMETER SPACE

Table B1 displays five entries of a tabulated library of the BP82-type wind solutions shown graphically in Fig. 1. The complete table is available electronically as Supporting Information for this article and via the VizieR data base of astronomical catalogues.

SUPPORTING INFORMATION

Additional Supporting Information may be found in the online version of this article:

Table B1. Global, self-similar (BP82-type) wind solutions in tabular form.

Please note: Wiley-Blackwell are not responsible for the content or functionality of any supporting materials supplied by the authors. Any queries (other than missing material) should be directed to the corresponding author for the article.

appear explicitly in the normalized equations for the disc structure (Section 2.1), but it is used in matching the disc solution to a self-similar wind solution (via equations 62 and 63). We have verified that this constraint is satisfied by the matched disc/wind solutions presented in Section 4.3.

This paper has been typeset from a TeX/LaTeX file prepared by the author.